Natural Hazards
https://doi.org/10.1007/s11069-025-07200-8

ORIGINAL PAPER

# Effective prediction of earthquake-induced slope displacements, considering region-specific seismotectonic and climatic conditions

**Danny Love Wamba Djukem[1] · Xuanmei Fan[1] · Hans-Balder Havenith[2]**

Received: 16 December 2024 / Accepted: 19 February 2025


**Abstract**
The Newmark displacement (ND) method is a reliable tool for assessing earthquake-induced slope deformation, yet a universally accepted regional-scale approach is still lacking. Existing ND equations often rely on regression from diverse strong-motion datasets or landslide statistics that were initially unavailable. To address this, we propose a site-adaptable ND approach (SAND) for various tectonic mountainous environments and scales. This knowledge- and data-driven method models cumulative slope displacement assuming normal pre-earthquake conditions, considering a quadratic relationship with peak ground acceleration (PGA) and a non-linear relationship with critical acceleration ($A_c$). We gradually incorporate region- and site-specific conditions, including fault type, focal mechanism, hanging/footwall effects, topographic amplifications, terrain roughness, and wetness coefficient. Case studies include landslides triggered by the Haiti earthquakes in 2010 and 2021, as well as those from Taiwan (1999), Lushan (2013 and 2022), and Luding (2022). SAND outperforms previous regression-based models in predicting landslide locations. The SAND threshold varies between 0 and 10 cm, in line with previous studies. The SAND approach quickly predicts shallow ETLs to support rescue efforts, using data on earthquake magnitude, epicenter, and focal mechanism (ideally the fault activated segment).

**Keywords** Critical acceleration · PGA distribution · Quadratic relationship · Newmark displacement · Haiti · Sichuan Province

## 1 Introduction

Large earthquakes are typically associated with, but not limited to, strong ground shaking, surface rupture, liquefaction, and, in mountain regions, widespread ETLs. ETLs account for a significant proportion of total earthquake losses in mountainous areas, particularly in

✉ Xuanmei Fan
fxm_cdut@qq.com

[1] State Key Laboratory of Geohazard Prevention and Geoenvironment Protection, Chengdu University of Technology, Chengdu 610059, China

[2] Geology Department-B18, Georisk and Environment, Liege University, Sart Tilman, 4000 Liege, Belgium

the context of global population growth, settlements, and infrastructure (Fan et al. 2018; Havenith et al. 2022; Shao et al. 2022b; Zhao et al. 2023). These mountainous areas are vital for human and economic development globally. A single catastrophic earthquake in these regions can have widespread impacts, affecting the financial stability and sustainability of communities worldwide.

Frequently used earthquake-landslide assessment susceptibility methods as assembled by Shao et al. 2022b include mechanical models, heuristic or index-based approaches, statistical analysis methods, machine learning and deep learning models. The Newmark method has been used for almost 60 years to model the movement of a landslide assimilated to a block sliding on an inclined plane during an earthquake (Newmark 1965). This method aims at calculating the ND by using as inputs the record of local seismic shaking and the critical acceleration ($A_c$); the latter is defined as the ground acceleration necessary to trigger first slope movements (Wilson and Keefer 1983; Jibson 1993; Jibson and Keefer 1993; Ingles et al. 2006; Du and Wang 2016; Cui et al. 2019; Jin et al. 2019; Yiğit 2020). Initially, this physics-based model was developed to assess co-seismic permanent displacements and related slope failure probability for specific sites. Later, the Newmark method was adapted for the spatial analysis of seismically induced slope deformation at a regional scale by, e.g., Jibson et al. (1998), Jibson et al. (2000), Jibson et al. (2004), Jibson et al. (2006)); Chen et al. (2019); Jin et al. (2019); Djukem et al. (2024). The adaptation to regional analyses required several adaptations and considerations. One important factor is the attenuation of the seismic intensity at variable distances from the seismic source. Further, various geo-environmental factors need to be integrated in the analysis, such as detailed topographic and geological information (Yang et al. 2024).

The goal of the 'spatial' prediction of NDs is to outline areas with a higher or lower probability of co-seismic landslide occurrence. Compared with other—purely statistical—techniques used for regional landslide susceptibility assessment, the spatial variant of the Newmark method has the advantage that its application does not depend on the availability of a landslide inventory. Therefore, this method can be implemented more quickly than statistical methods (Havenith et al., 2022; Shao et al. 2022a; Djukem et al. 2024) once information is available on the magnitude of the earthquake, its epicenter, hypocenter, and the location of the activated seismogenic fault (Jibson 2011; Cui et al. 2019; Ma and Xu 2019; Chen et al. 2023; Yang et al. 2024).

However, the current trend in applying the ND method can be summarized by the assertion that the predictive capability of the newly developed ND equations surpasses the existing formulations. The adaptability of these equations for predicting future ETLs in the same regions or not is not considered. Most statistically derived ND equations are calibrated using strong-motion datasets and landslide inventories from specific seismic events. They are then applied to future earthquakes, often in different tectonic settings, without sufficient validation. However, their predictive capability in new regions remains questionable. Djukem et al. (2024) compared two ND equations—the Miles and Ho (1999) or M99 equation, originally derived for California, and the Jin et al. (2018) or J18 equation—following the 2022 Mw 6.8 Luding earthquake in southwestern China. Surprisingly, the M99 equation outperformed J18 in capturing landslide distribution, even though J18 was developed more recently. This suggests that older equations, despite being site-specific, can sometimes generalize better than newer ones that rely more heavily on statistical correlations.

It should also be noted that the coefficient variations in ND equations are seldom explained by regional specificities. These changes often appear random, driven by statistical correlations from earthquakes and landslide records that are not initially available.

Wang et al. (2014) attempted to include triggering and environmental factors in the ND analysis after the 12 May 2008 Wenchuan Earthquake in the Pingwu County of Sichuan Province, China. But they used one of these empirical ND formulas proposed by Hsieh and Lee (2011). The coefficients in the ND equation were derived through regression analysis of strong-motion data from various seismic events that took place in regions with different geological, geomorphological, hydrogeological, and tectonic conditions. These events included the 1995 Kobe earthquake, 1999 Kocaeli earthquake, 1999 Chi-Chi earthquake, 1999 Duzce earthquake, 1994 Northridge earthquake, and the 1989 Loma Prieta earthquake.

The calculation of ND can be done by considering either the Arias intensity ($I_A$) or the PGA as a seismic parameter. But so far, the conditions for using one or the other seems to remain unclear. However, PGA is generally more readily available immediately after an earthquake compared to $I_A$ (Tsinidis et al. 2019; Hsu and Pratomo 2022). Moreover, during an earthquake, ground acceleration fluctuates over periods typically lasting several tens of seconds, making the absolute maximum value recorded on an accelerogram, known as PGA, the most critical parameter for assessing ETLs as highlighted by Power et al. (2012); Yuan et al. (2013); Du et al. (2018); and Yao et al. (2020). In the absence of seismic recorded data, already available ground motion prediction equations or shake maps are made available few minutes after a seismic event (Tsinidis et al. 2019). PGA empirical equations account for source distance, magnitude, and site geology, allowing for the assessment of key factors that influence earthquake damage. They also incorporate the effects of the hanging and footwall site of seismogenic faults on PGA attenuation (Ambraseys et al. 1996; Abrahamson and Silva 2007; Campbell and Bozorgnia 2007; Chiou and Youngs 2007; Houqun et al. 2016).

Therefore, it seems essential to reevaluate the effectiveness of ND models in different tectonic environments to derive the conditions that determine the effectiveness of this method. We propose a site-adaptable approach (SAND), which allows rapid calculation of probable slope displacements in different tectonic environments and scales. The predictive capacities of SAND models are compared with the PGA-based ND regression equation proposed by Jin et al. (2019), called J19. The case studies include 6 earthquakes and their associated landslides. These are the Mw 6.7 Lushan 2013, Mw 5.9 Lushan 2022, Mw 6.8 Luding 2022, and the Mw 7.5 Chi-Chi 1999 events for China, and the Mw 7.0 Port-au-Prince 2010 and Mw 7.2 Nippes 2021 earthquakes for Haiti.

## 2 Study areas

### 2.1 Natural settings and landslides

The hilly and mountainous terrain of the western Sichuan (Lushan and Luding areas) and Taiwan in China, along with the southern regions of Haiti, are regions that frequently experience $M > 6.5$ earthquakes (Wen et al. 2004; Gorum et al. 2013; Bai et al. 2018; Fan et al. 2018; Ma and Xu 2019; Havenith et al. 2022). Related events are often accompanied by coseismic landslides (Fig. 1), which account for a significant percentage of total earthquake damages. Type and distribution of triggered landslides depend on several regional and site-specific seismological, geological, climatic, and geomorphological factors, including the effect of diverse fault mechanisms (Keefer 2002; Meunier et al. 2008; Gorum et al. 2013; Havenith et al. 2022; Shao et al. 2022b).

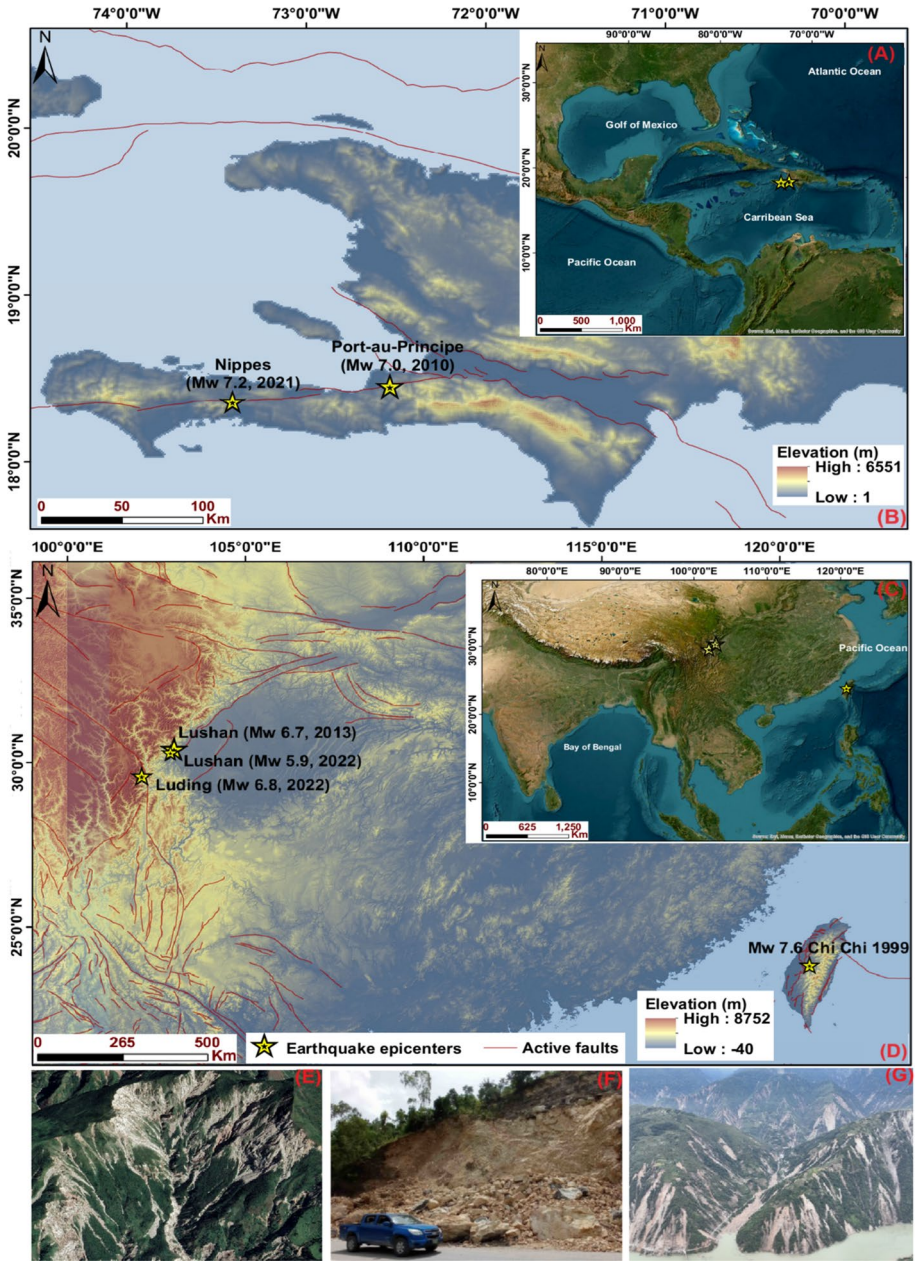


**Fig. 1** Seismotectonic context and location of Haiti, Lushan, Luding, and Taiwan (**A**, **B**, **C** and **D**); coseismic landslides in Haiti (**E** and **F**) and China (**G**). The red lines depict the global active fault system, sourced from the Global Active Faults Database (https://www.globalquakemodel.org/gem-active-faults-database)

Yuan et al. (2016) highlighted that the earthquake's focal mechanism indicates the direction of seismic wave propagation and the tectonic stress distribution in the source-surrounding region. Tang et al. (2023) emphasized that the stress field propagation is

different for reverse, normal or strike-slip fault activation. However, for all types of faults, the strongest shaking is always expected to occur within the hanging wall. We can define hanging wall for reverse or normal faults, but not for strike-slip faults. This was highlighted by the Wenchuan earthquake, which had induced far more landslides (and larger ones) on the eastern hanging wall side of the activated fault segments than on the western foot wall side (Qi et al. 2010).

The Lushan and Luding have experienced recurrent earthquakes without any significant pre-earthquake meteorological event over the years. The island of Taiwan has experienced one major earthquake in September 1999, with significant typhoons before and after this event of magnitude 7.7 (Fig. 1). The southwestern part of Haiti has been crossed by hurricanes a few years before and directly after the 2021 event (Havenith et al. 2022; Amatya et al. 2023), while the region affected by the 2010 earthquake had not been affected by hurricanes before or after the event. The earthquake-affected region had not experienced a major hurricane for about six years before the 2010 event. The most recent major hurricane prior to the earthquake was Hurricane Jeanne in 2004. The earthquakes, ETLs, geoenvironmental conditions and population density of these regions selected for our study are shown in Table 1.

### 2.2 Tectonic settings and ETLs of Haiti, Lushan, Taiwan, and Luding

The seismogenic fault systems, earthquakes, and earth-induced landslides of the targeted parts of Haiti, Taiwan, Lushan, and Luding are presented.

#### 2.2.1 Haiti

The Mw 7.0 Port-au-Principe 2010 (January 12) and the Mw 7.2 Nippes 2021 (August 14) earthquakes occurred on fault segments (marked by oblique thrust and strike-slip fault movements) associated with the Enriquillo-Plantain Garden strike-slip fault system (Havenith et al. 2022).

This fault system is located near the North American-Caribbean plate boundary (Fig. 1A) characterized by a complex tectonic evolution due to an oblique subduction taking place in the east, and a transform plate boundary in the west, increasing its seismicity potential (Prentice et al. 2010; Bakun et al. 2012; Possee et al. 2020). The historical seismicity revealed that the Port-au-Prince region (southern Haiti) has experienced earthquakes of magnitudes 7.0 or greater several times (Bilham 2010; Calais et al. 2010). These include the events of September 15 and November 21, 1751. with one having a modified Mercalli intensity of X. Also, the largest earthquakes occurred in 1770 (3 June) and 1860, with their assumed epicenters at 30–50 km more to the west on the Enriquillo-Plantain Garden fault (Fig. 2A). After about 200 years of relatively low seismic activity, a disastrous earthquake of magnitude Mw 7.0 struck the Port-au-Prince region of Haiti on January 12, 2010 (Bilham 2010; Calais et al. 2010). This event resulted from the combined rupture on the Léogâne blind thrust fault and a deep lateral slip on the Enriquillo-Plantain Garden Fault as concluded by Calais et al. (2010); Gorum et al. (2013) and Kocel et al. (2016). This earthquake was followed by more than 59 aftershocks of magnitude 4.5 or greater. About 300,000 people had been killed and, more than a million had to be relocated (Calais et al. 2010; DesRoches et al. 2011; Gorum et al. 2013; Havenith et al. 2022). More than 20,000 landslides (mostly shallow rock and debris falls) at a maximum distance of 46 km from the epicenter were inventoried by Harp et al. (2016), and 5000 landslides were

**Table 1** Earthquake, associated ETLs and pre-earthquake meteorological events

| Region/date/ magnitude | Fault types | Depth (km) | Pre-earthquake event | Landslide polygons | Areas ($km^2$) | Population density |
|---|---|---|---|---|---|---|
| Mw 6.7 Lushan 20 April 2013 | Blind reverse fault | 10 | No significant | 2820 | ~20 | 270/$km^2$ (2017) |
| Mw 5.9 Lushan 1st June 2022 | Thrust faul | 14 | Rainfall (May 6 to June 5) | 1091 | ~5 | 270/$km^2$ (2017) |
| Mw 6.8 Luding 5 Sept 2022 | Left-lateral strike-slip fault | 16 | No significant | 5769 | ~33 | 23/$km^2$ (2019) |
| Mw 7.5 Chi Chi 31 July 1999 | Left-lateral strike-slip fault | 7 | 1996 Typhoon Herb | 13,783 | ~230 | 673/$km^2$ (2023) |
| Mw 7.0 Port-au-Principe 12 January 2010 | Combined blind thrust and strike-slip faults | 13 | No particular event | ~235 666 | ~33 | 414/$km^2$ (2023) |
| Mw 7.2 Nippes 14 August 2021 | | 10 | Hurricane Matthew 28 Sept to 10 Oct 2016 | 8104 | ~60 | 414/$km^2$ (2023) |

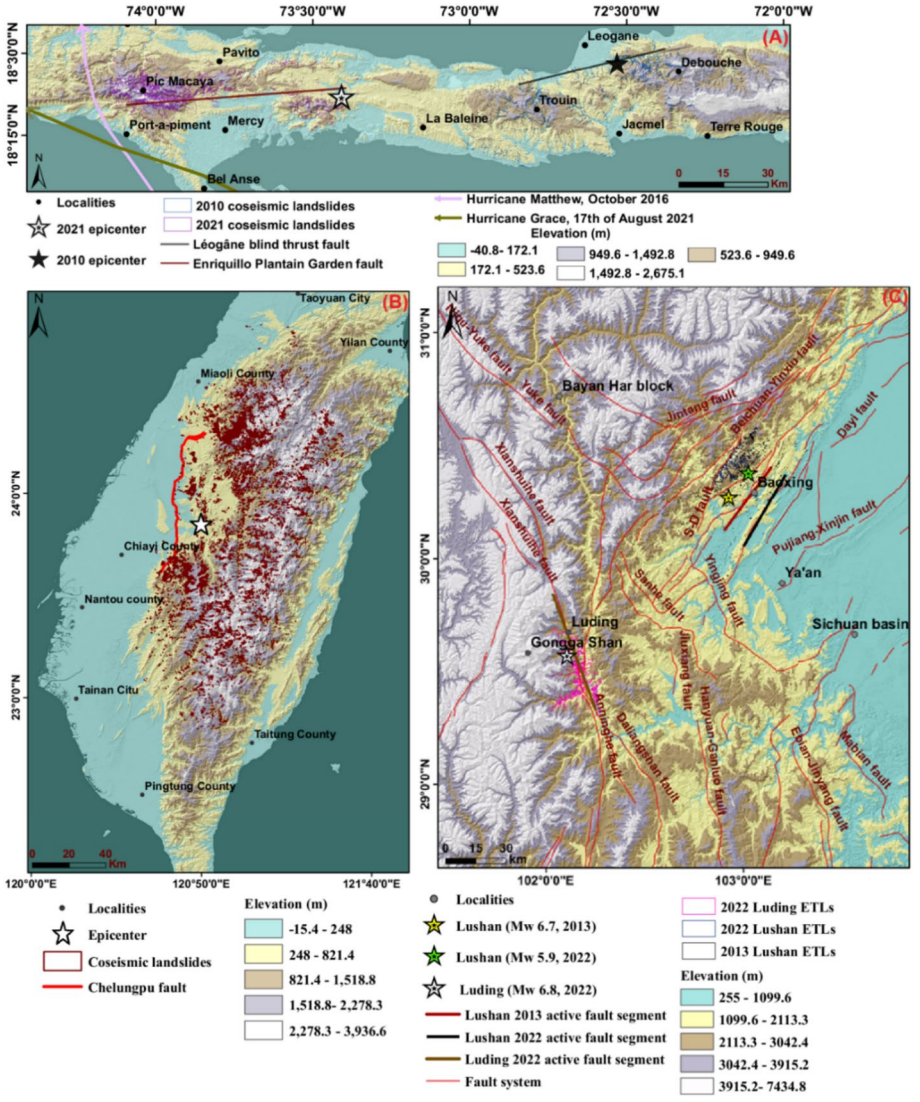


**Fig. 2** Overview of the study areas: **A** southern part of Haiti: ETLs' inventories of a representative region with two earthquakes and Hurricanes. The 2021 coseismic landslide inventory has been modified from Havenith et al. (2022). The 2010 landslide catalog is from Harp et al. (2016). **B** Spatial distribution of ETLs triggered by the 1999 Chi Chi earthquake in Taiwan. The Chelungpu fault and epicenter have been digitized from Chuang et al. (2020). **C** the fault system in the Luding and Lushan areas. The fault lines are extracted from Wu et al. (2023); the elevation map is derived from the Copernicus global digital elevation models provided by OpenTopography

mapped by Gorum et al. (2013). Detailed investigations of the January 12 Haiti earthquake indicated the absence of any surface ruptures of the activated Léogâne Fault near the Enriquillo-Plantain Garden fault (Bilham 2010 and Calais et al. 2010).

More recently, the August 14, 2021, Mw 7.2 Nippes earthquake had its epicenter located near the Enriquillo-Plantain Garden fault surface expression, at about 150 km

in the west of Port-au-Prince. This 2021 earthquake struck the same broader fault zone as the 2010 Mw 7.0 earthquake and did not produce a clear surface rupture. This main earthquake was followed by several aftershocks with a magnitude of up to Mw 5.7. During this event, approximately 2500 people were killed, 13,000 were injured and more than 137,000 structural failures had occurred (Calais et al. 2022); about 8000 landslides had been triggered by this earthquake (inventory of Havenith et al. 2022, used for this study).

### 2.2.2 The island of Taiwan

Taiwan is located between the Philippine Sea plate and the Eurasian plate, which moves to the northwest, resulting in lateral compression (Fig. 1E). Small seismic tremors affect the island of Taiwan almost daily (Chen and Hawkins 2009; Chuang et al. 2020). Taiwan is located at 175 km east of the mainland China. The target area is characterized by elevations ranging from about 0 to 4000 m. The study area extends from about longitudes 120° to 122°E and latitudes 22 to 25°N (Fig. 2B).

The destructive Mw 7.6 Chi-Chi earthquake of September 21, 1999 produced an approximately 100 km long surface rupture with variable strikes, along the Chelungpu fault. The Chelungpu fault dips superficially to the east (Huang 2000; Ma et al. 2001). Boore and Atkinson (2008), Chiou and Youngs (2008), Idriss (2008), and Hsieh and Lee (2011) highlighted that seismic ground motion attenuates faster in Taiwan, leading to low ND values even for large movements occurring far from the fault. This rapid attenuation is influenced by Taiwan's complex geological setting, soil properties, and tectonic environment, all of which play a crucial role in shaping landslide distribution. Taiwan's geological complexity, resulting from the convergence of the Philippine Sea and Eurasian plates, features diverse rock formations and fault systems, such as the Chelungpu fault, whose thrust faulting mechanisms contribute to rapid energy dissipation. Additionally, soft soil in areas like the Taipei Basin influence attenuation by initially amplifying seismic waves but later increasing energy dissipation due to their non-linear behavior. The tectonic environment further contributes to this phenomenon, as strong ground motions near the fault diminish quickly due to wave scattering and absorption by varied geological formations. These attenuation characteristics affect landslide triggering by shaping the intensity and duration of seismic shaking, leading to spatial variability in landslide distribution. Regions with softer soils experience different landslide dynamics than those on harder substrates due to variations in seismic energy dissipation.

More than 20,000 landslides have been triggered during this event (Huang 2000; Khazai et al. 2004). The landslide catalogue (Fig. 2B) used for this investigation is from Huang (2000).

Most of these landslides were shallow debris slides and rock avalanches that occurred across a 150 $km^2$ area as highlighted by Dadson et al. (2004); Lin et al. (2006). The July 31 to August 1, 1996, typhoon Herb event, which crossed the northern part of the island 3 years before the Chi-Chi earthquake triggered a total of 73 debris flows. Typhoon Herb (1996) brought significant rainfall to Taiwan, with some areas receiving up to 1,199 mm of precipitation over 24 h (Wu and Kuo 1999). While the July 29–31, 2001, Toraji typhoon event recorded a total precipitation of 757 mm but triggered more than 300 debris flows.

### 2.2.3 Lushan and Luding tectonics under the influence of the western Sichuan faults

Earthquakes in the western Sichuan China occur, mainly along the Longmenshan and Xianshuihe fault systems (XSHF). The Longmenshan fault system (Fig. 2C) is a thrust boundary along the eastern margin of the Tibetan Plateau, which consists of three major faults from west to east. These are: the Wenchuan-Maoxian, Yinxiu-Beichuan, and Anxian-Guanxian fault, respectively (Wen et al. 2004; Xu et al. 2008; Zhang et al., 2013; Guo et al. 2024). The eastward extrusion of the Tibetan Plateau and the obstruction of the Sichuan Basin justify the complex tectonic setting of the Longmenshan mountains. This leads to high active seismicity along the Longmenshan fault system, where several devastating earthquakes have been recorded in the past, including the May 12, 2008, Ms 8.0 Wenchuan earthquake epicenter located in the Longmenshan mountains, in areas with similar geographical, geological, and geomorphological conditions with the Lushan 2013 earthquake (Li et al. 2013).

The April 20, 2013 Mw 6.7, and the June 1, 2022, Mw 5.9 Lushan earthquakes resulted from the rupture of the Longmenshan blind thrust fault zone through a blind reverse focal mechanism as concluded by Hao et al. (2013); Xu et al. (2013); Yuan et al. (2016); and Duan et al. (2022). Luo et al. (2015), after analyzing the seismic records of 37 aftershocks of the 2013 Lushan earthquake with magnitudes ranging from Mw 3.4 to 5.1, confirm that the focal mechanisms predominantly indicate thrust events. But they also found occasional strike-slip mechanisms. The 2013 Mw 6.7 Lushan had its epicenter located at the south end of the Longmenshan fault zone, about 100 km from the Wenchuan earthquake epicenter. The Mw 5.8 Lushan earthquake in 2022 occurred along the southern segment of the Longmenshan trust tectonic zone, in Baoxing County, Ya'an City (Fig. 2C). The epicenter was located at 30.395N, 102.958E with a focal depth of about 12.0 km (Zhao et al. 2022). Tang et al. (2023) highlighted that this earthquake occurred in the seismic gap between the previous 2013 Lushan and the 2008 Wenchuan earthquakes.

Moreover, the epicenter of the September 5, 2022, Mw 6.8 Luding earthquake was located on the Moxi fault, a single and linear segment of the SE Xianshuihe Fault (An et al. 2023; Dai et al. 2023). The Moxi fault is in the intersection between the Xianshuihe fault and the Longmenshan Fault systems (Fig. 2C). This zone is found between strike-slip fault zones encompassing the Garze-Yushu, Xianshuihe, Anninghe, Zemuhe, Xiaojiang, Jinsha River faults; and the Longmenshan thrust fault Zone (Allen et al. 1991; An et al. 2023).

## 3 Data and method

We present the process of acquisition of the datasets necessary to compute the slope factor of safety (FS), critical acceleration ($A_c$), peak ground acceleration (PGA), and Newmark displacement models (ND). The 30 by 30 m digital elevation models (DEMs) of the targeted regions have been provided by the European Space Agency distributed by OpenTopography (https://opentopography.org/). The following geoenvironmental factor maps have been used: slope, slope aspect, distance to river, and curvature. The seismic factors include the PGA, amplified PGA, PGA attenuation, epicentral and hypocentral distance maps. The soil-rock geomechanical properties included cohesion (c), friction angle ($\Phi$), and material unit weight ($\gamma$). The hydrogeological condition of these slopes affects their mechanical properties, the degree of mobilization, and the volume of these materials as

highlighted as Li et al. (2016); Kharismalatri et al. (2019); and Pudasaini and Krautblatter (2021). This hydrogeological influence is considered by integrating the wetness coefficient (m) in the calculation of the critical acceleration ($A_c$).

### 3.1 Landslide datasets

The landslide inventories used to evaluate the predictive ability of the computed ND models are from different sources. Landslide catalogs for the 1999 Chi Chi earthquake in Taiwan and the 2010 Haiti earthquake are from Liao and Lee (2000) and Harp et al. (2016), respectively.

The 1999 Chi Chi earthquake in Taiwan triggered approximately 13,783 landslides over an area of approximately 230 $km^2$. For the 2021 Haiti event we use a revised version of the ETL catalog presented by Havenith et al. (2022). Some polygons erroneously identified as landslides have been removed from this catalog, while others were manually added based on the visual interpretation of 30 Planet Scope satellite images of 3 m resolution. The acquisition dates of the images are presented in the Supplementary table (Table S1). We had to download several images taken at different times in some places marked by extensive cloud cover. An overview of the southern part of Haiti before and after the 2021 earthquake has been reconstructed by juxtaposing these satellite images (Fig. S1 of the supplementary material).

The 2013 and 2022 Lushan ETLs have been automatically extracted through the interpretation of satellite imagery. We have juxtaposed the Spot-5 satellite data for the period of June 7 and 28; July 16 and 29, for the 2013 ETL inventory. The 2022 Lushan ETLs inventory has been derived from Planet Scope satellite data taken on July 6, 2022 (Fan et al. 2022; and Dai et al. 2023). The acquisition dates of the satellite images used to extract ETLs are presented in Table S1. The resulting ETL maps are presented in the supplementary material Figs. S2.

### 3.2 Geoenvironmental and seismic factors necessary to compute ND models

The methods used to generate slope, slope aspect, curvature, lithological maps (Supplementary materials Figs. S3, S4, S5, S6) and distance to faults are identical to those described in Djukem et al. (2020 and 2024).

#### 3.2.1 Lithological formations

Lithological maps of Luding, Lushan and Taiwan (Figs. S6) were extracted from the 1:200 000 global lithological map database GLiM compiled by Hartmann and Moosdorf (2012).

**3.2.1.1 Haiti** The island of Hispaniola is dominated by magmatic and sedimentary rocks. These are: cretaceous andesitic to silicic volcanic rocks, cretaceous volcanic rocks, carbonate sedimentary, and alluviums. About 80% of the mountainous areas affected by the 2010 and 2021 earthquakes are made of (partly highly weathered) limestone. The lithological map of Haiti has been extracted from Havenith et al. (2022).

**3.2.1.2 Taiwan** Hartmann and Moosdorf (2012) and Lin and Chen (2016) have assembled several results to generate the lithological maps of Taiwan. The Island of Taiwan presents

magmatic (andesite, tuffs, volcanic breccia, basalt, ultrabasic rocks); metamorphic (gneiss, schist, metagranite, marble, and amphibolite), and sedimentary rocks (alluvium and terrace deposits; conglomerate, carbonate, or limestone).

**3.2.1.3 Luding and Lushan** Luding and Lushan are dominated by magmatic, metamorphic, and sedimentary rocks. These rocks include acidic plutonic, basic plutonic, basic volcanic, intermediate plutonic, intermediate sedimentary, pyroclastics, carbonate sedimentary, siliciclastic.

### 3.2.2 Soil-rock geomechanical properties

The ND scenarios computed consider shallow landslides with the sliding depth (t) of 5 m. The study areas are situated in sub-tropical regions with thick weathering crust which is likely to be similar for sedimentary, magmatic, and metamorphic rocks (M.A., 1991; White and Brantley 2003). Rodríguez-Peces et al. (2014) reported that, based on geotechnical data and laboratory tests, the average values for various rock types are: cohesion (c) 41 to 74 kPa; angle of internal friction ($\Phi$) 23 to 30°; and unit weight ($\gamma$) 18 to 26 kN/m$^3$. These rocks include micashists, quartzites, gneisses, phyllites, and different types of sedimentary rocks and soils such as limestones, dolostones, marbles, sandstones, and clays. The shear strengths parameters do not vary significantly with lithology. Therefore, geomechanical properties values of superficial soil-rock formations used to compute ND models are $c = 50$ kPa, $\Phi = 25°$, and $\gamma = 18$ kN/m$^3$. Similar values have been commonly used to predict the shallow landslides' Newmark Displacements in these regions, also in regions with similar geological formations (Cui et al. 2019; Djukem et al. 2024). These values are then assigned to all lithologies for the slope factor of safety (FS) calculations.

## 3.3 Implementing the site-adaptable ND approach (SAND)

### 3.3.1 Statistical regression and empirical equations

Hsieh and Lee (2010) highlighted that there are two tendencies regarding the application of the 'spatial' Newmark method at regional scale. The first consists of performing statistical regression from actual specific areas strong-motion records to estimate the slope displacement under seismic loading. The second is an empirical prediction of the ETLs using the already developed ND formulas.

Moreover, Jibson (2007) and Hsieh and Lee (2010) emphasized that the factors frequently used for ND models include an index for measuring seismic intensity (over the whole duration of the shaking) known as the Arias Intensity ($I_A$); some models also use the measure of the maximal ground movement at a given geographic point during an earthquake called PGA (peak ground acceleration) or $a_{max}$, and/or the magnitude of the earthquake ($M_w$); one or two of those measures are then combined with the critical acceleration ($A_c$) value to compute ND. Only five representative ND equations are presented in this work (Eqs. 1–5). They are, respectively, from Miles and Ho (1999); Jibson et al. (1998); Jin et al. (2018); Jin et al. (2019); and Rathje and Saygili (2009).

$$\log(ND) = 1.46 * \log(I_A) - 6.642 * A_c + 1.546 \tag{1}$$

$$\log(ND) = 1.521 * \log(I_A) - 1.993 * \log A_c - 1.546 \pm 0.375 \tag{2}$$

$$\log(ND) = 0.465 \log I_A + 12.896 A_c \log I_A - 22.201 A_c + 2.092 \pm 0.148 \tag{3}$$

$$\log(ND) = 0.215 + \log\left[\left(1 - \frac{0.7A_c}{PGA}\right)^{2.341} * \left(\frac{0.7A_c}{PGA}\right)^{-1.438}\right] \tag{4}$$

$$\begin{aligned} \ln ND = {} & 4.89 - 4.85\left(\frac{A_c}{PGA}\right) - 19.64\left(\frac{A_c}{PGA}\right)^2 \\ & + 42.49\left(\frac{A_c}{PGA}\right)^3 - 29.06\left(\frac{A_c}{PGA}\right)^4 + 0.72 \ln(PGA) + 0.89\left(M_w - 6\right) \end{aligned} \tag{5}$$

The general form of the preceding ND equations using either PGA or Arias $I_A$ can be summarized by Eqs. (6) and (7). The first term $X_1 \log I_A$ or $X_1 \log PGA$ represents the weight of the shaking intensity, the second term $X_2 A_c$ or $X_2 * \log(A_c)$ represents the weight of the critical acceleration ($A_c$), and the last term "$X_3$" represents the errors or uncertainties or variability of these variables' linearity for the computation.

$$\log(ND) = X_1 * \log I_A - X_2 * A_c + X_3 \tag{6}$$

$$\log ND = X_1 * \log PGA - X_2 * A_c + RF \tag{7}$$

Newmark (1965) and Jibson (2011) pointed out that the dynamic shear resistance and the static shear resistance are nearly equal (a statement that we take here as given but which for sure might also be debated as indicated by Yang et al. 2024); and that the safety factor in this state is large enough to prevent significant movement in all compacted embankment materials and in several natural soil layers. In addition, faults are typically in a state of static equilibrium before an event, with static shear stresses balanced by frictional resistance (Day et al. 1998). This equilibrium is factored into the static factor of safety calculations.

### 3.3.2 Assumptions considered in the SAND approach and key factors' interaction

The SAND approach combines the knowledge-driven and data-driven approaches. Following these pre-earthquake state of equilibrium statements, our ND models are implemented based on Eq. (8), which with the coefficient 2, initially assumes an equal interaction between seismic and geo-environmental factors, prior to an earthquake event.

$$\log ND = 2 \log PGA - 2A_c + RF \tag{8}$$

In which, PGA incorporates magnitude, amplified curvature, amplified slope aspect, HW/FW effect; $A_c$ incorporates distance to rivers converted into wetness coefficient (m); RF is the ruggedness coefficient. We introduce a ruggedness or roughness factor (RF), to account for the pixels neighboring values, in place of the uncertainty term used in the statistical regression.

The coefficient of 2 for the term logPGA also implies that the Newmark Displacement is proportional to the square of PGA since $10\exp(2\log PGA) = (PGA)^2$. This assumes a quadratic relationship between ND and PGA, and non-linear with $A_c$, since the equation is in logarithmic form.

The quadratic relationship has long been applied in several domains including: seismic risk analysis for the detailed representation of the large magnitude-low frequency region (Merz and Cornell 1973); in electromagnetic geophysical surveys for electromagnetic data correction (Santos and Porsani 2011), for evaluating the relationships between macroseismic intensity, PGA, peak ground velocity (PGV) and the spectral acceleration (Oliveti et al. 2022). Similarly, Jang et al. (2023) demonstrate the effectiveness of quadratic programming in optimizing ground motion models, while Robinson et al. (2017) highlight its role in predicting landslide frequency based on PGA and distance from rivers. Li et al. (2024b) further emphasize the necessity of nonlinear approaches to capture seismic slope responses, and Chan and Chen (2024) advocate for hybrid statistical-physical models to improve landslide hazard assessments. These studies collectively underscore the importance of quadratic and nonlinear relationships in understanding complex geophysical and geotechnical processes.

### 3.3.3 Theoretical framework explaining why quadratic relationships might emerge from the underlying physical processes involved in ETLs

**3.3.3.1 The fundamental physics of energy transfer and work done by seismic forces** The quadratic relationship with PGA (2logPGA) can be justified by considering the complex (non-linear) interactions conditioning seismic energy transfer and dissipation (Carey et al. 2019; Li et al. 2021b; Shao et al. 2022b; He et al. 2021). In this case, the ETLs predisposing factors include magnitude, fault types, focal mechanism, hanging wall/footwall effect, amplified curvature and slope aspects. During an earthquake, the energy is transferred through seismic waves, which interact with slopes. The energy dissipation in the slope material follows a non-linear relationship (Carey et al. 2019; Li et al. 2021b), potentially quadratic, as the intensity of shaking increases as highlighted by Oliveti et al. (2022).

**3.3.3.2 Topography, pore pressure effects and amplification non-linearity** As highlighted by Li et al. (2021b), faults, joints, and bedding planes create discontinuities that can facilitate or inhibit landslides in ways that are difficult to predict linearly. Also, slope angle, aspect, and curvature influence landslide susceptibility non-linearly. Steeper slopes are generally more prone to failure, but very steep slopes may have already shed unstable material.

Moreover, pore pressure generation during shaking can reduce effective stress non-linearly, potentially leading to quadratic relationships between displacement and ground motion parameters. In addition, topographic and soil amplification of seismic waves can lead to non-linear increases in ground motion with increasing input motion, potentially resulting in quadratic relationships (Boore and Atkinson 2008; Jang et al. 2023).

**3.3.3.3 The relationship between strain energy and the difference between driving and resisting forces** The inertial forces acting on a potential landslide mass are proportional to acceleration.

The quadratic $A_c$ term might represent a non-linear relationship between slope stability and wetness, where small changes in wetness near a critical threshold have outsized effects on stability. In this sense, He et al. (2021) highlighted that pore water pressure

significantly affects slope stability, but its distribution and changes during seismic shaking are highly non-linear. Moreover, antecedent rainfall can increase landslide susceptibility, but its effects depend on complex interactions with soil properties and topography (Carey et al. 2019).

This theoretical framework suggests that quadratic relationships could emerge due to interaction between slope displacement geoenvironmental, hydrogeological and seismic conditions. Geoenvironmental, hydrogeological and seismic factors vary for Haiti, Lushan, Luding and Taiwan. The site-adaptable ND model is therefore implemented based on Eq. (8). The general ND model calculation flowchart is presented in Fig. 3.

The ND is therefore computed following a three-step approach (Fig. 3). First the slope factor of safety and critical acceleration are computed following Eqs. (9) and (10), as presented in Fig. 3. Second, the influence of water on these slopes' stability is considered by computing and integrating the wetness coefficient map (Fig. S7). Third we compute the peak ground acceleration (PGA) following attenuation laws that account for several influential factors, namely: PGA attenuation factors, ruggedness coefficient and amplification factors (fault focal mechanism, curvature, and slope aspect). The details of this ND computation steps are presented below.

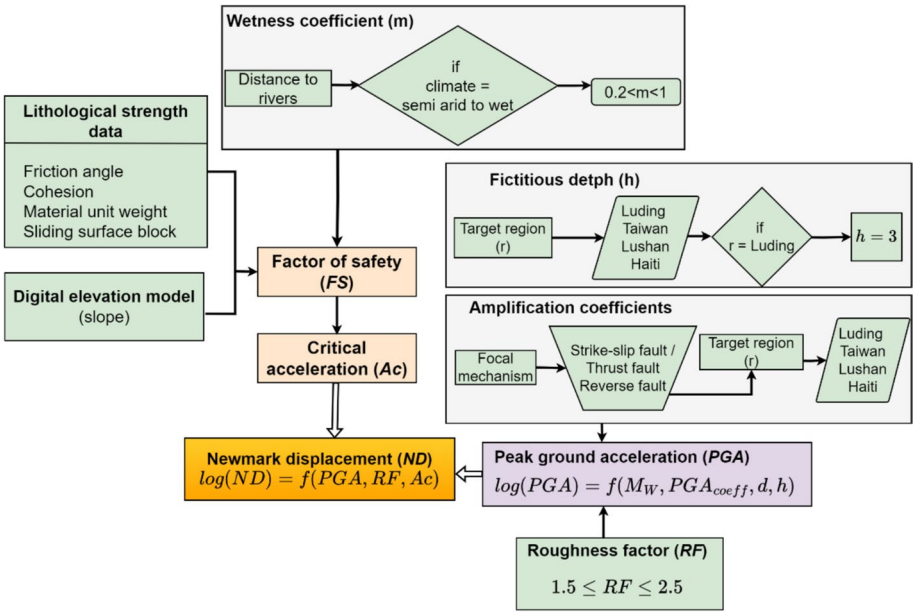


**Fig. 3** The steps for the calculation of the site-adaptable Newmark displacement (SAND). $A_c$ and FS consider the wetness coefficient (m). The PGA accounts for the roughness factor (RF), PGA attenuation factor (H) and the amplification factors. The detailed calculation steps of "m", amplification factors, and assignment of the PGA attenuation factors are developed in Figs. S6, S7, and S8

### 3.4 Computation of FS and $A_c$

The infinite slope model was assumed in computing the FS (Eq. 9) as applied before in these regions or similar ones by Ward et al. (1982), Jibson et al. (2000); Chen et al. (2012); Jin et al. (2018); Huang et al. (2020); Chen et al. (2023); Gong et al. (2023); Djukem et al. (2024); Li et al. (2024a, b). Equations (9) and (10) were implemented using the raster calculator tool in ArcGIS 10.8. The slope angle (α), cohesion (c), friction angle $(\emptyset)$, unit weight $(\gamma)$, the depth of the sliding surface (t), and the wetness (m), are essential for the FS and $A_c$ calculation.

$$FS = \frac{c}{\gamma \times t \times \sin\alpha} + \frac{\tan\emptyset}{\tan\alpha} - \frac{m \times \gamma_w \times \tan\Phi}{\gamma \times \tan\Phi} \tag{9}$$

$$A_c = (FS - 1) \times g \times \sin\alpha \tag{10}$$

#### 3.4.1 Computation of FS and $A_c$ considering the wetness coefficient

Climate, through temperature, precipitation and soil moisture, plays a critical role in predisposing slopes to failure during earthquakes (Havenith et al. 2022; Loche et al. 2022). Similarly, deeply incised river channels can influence groundwater level fluctuations associated with intense soil wetting and drying phenomena that cause slope instability even in the absence of seismic shaking. In addition, an increase in hydrostatic pressure can lead to a total or partial loss of shear strength under shaking conditions or with even small deformations (Newmark 1965; Dai and Lee 2003; Kharismalatri et al. 2019; Djukem et al. 2020; Pudasaini and Krautblatter 2021).

The difficulty in determining the spatial and temporal patterns and controls of ETLs by climate zone is that the authors do not always specify the type of climate in the study areas. Therefore, we used the geographic distribution of wet and dry climate zones created by Li et al. (2021a) to differentiate climate zones. This classification is based on soil moisture using the 30-year average of soil root zone temperature with the reference period of 1976–2005. Lushan and Luding have a semi-arid climate; Haiti and Taiwan have a subhumid/humid climate. High and frequent rainfall in tropical areas, often characterized by a bimodal annual pattern, leads to faster saturated soil conditions. Therefore, we assumed the wetness coefficient (m) to vary between 0.2 and 1 in subarid/arid climate (Luding and Lushan), and between 0.6 and 1 in subhumid/humid climate or humid tropical climate influenced by typhoons and hurricanes (Haiti and Taiwan).

Distances from major rivers were computed using the Euclidean distance tool of ArcGIS 10.8 around river networks extracted from the DEM. The resulting map was converted into wetness coefficient (m) maps, assuming that the distance classes closest to the hydrographic networks were the most likely to favor landslide occurrences as reported by Havenith et al. (2016); Djukem et al. (2020); Tseng et al. (2022). The weighting was done by using the heuristic fuzzy logic approach previously applied by Djukem et al. (2020); Badola et al. (2023); Zhang et al. (2023).

The fuzzy logic theory developed by Zadeh in 1965 has proven effective for creating landslide susceptibility maps on a regional scale. This approach is particularly useful because it can handle the inherent uncertainty and vagueness associated with landslide events and their contributing factors. Fuzzy logic allows for a more nuanced representation of the complex relationships between various environmental variables that influence

landslide occurrence, providing a more accurate assessment of landslide risk across large areas (Badola et al. 2023; Zhang et al. 2023).

In this investigation the membership degree (y) in fuzzy logic indicates how the distance to rivers (x) influences landslide susceptibility. For $y = 1$, the distance to river strongly increases landslide risk; $y = 0$, the distance to river has minimal impact on landslide risk, and for $0 < y < 1$, the distance to river has an uncertain influence on landslide risk. As the membership degree (y) increases for a given distance on the distance to river map (x), it suggests a higher landslide susceptibility for that area. The distance to river maps were therefore converted into fuzzy subsets with values ranging from 0.2 to 1 in semiarid climate (Luding and Lushan) and from 0.6 to 1 in humid tropical climate influenced by typhoons and hurricanes (Haiti and Taiwan). The assignment of a fuzzy subset or weight to each distance to river class was done under the assumption that high and frequent rainfall in tropical areas may lead to faster saturated soil conditions than in semiarid regions. This operation was performed using linear fuzzy functions from the Spatial Analyst tools' Fuzzy Membership option in ArcGIS 10.5. We set membership values between 0.2 or 0.6 as the minimum, and a membership of 1 as the maximum. The commonly used wetness (m) of Eq. 9 has therefore been replaced by these wetness coefficients in the calculation of FS (Fig. S7). Figs. S8 shows the resulting wetness coefficient maps used to calculate FS.

### 3.4.2 Computation of the amplified peak ground acceleration

PGA is obtained through the following methods: strong-motion accelerometers, seismic hazard maps, attenuation relationships developed in forms of equations that predict PGA based on factors like earthquake magnitude, distance from the fault, and local site conditions (Wan et al., 2023). An attenuation law of the peak horizontal ground acceleration (Eq.11) is an empirical relationship that allows the value of ground motion generated by a given modeled earthquake to be predicted at any given map pixel. The Eqs. (11) and (12) proposed by Ambraseys et al. (1996) consider the source-distance, surface wave magnitude, and site geology. Equation (12) is suitable for magnitudes 4.0–7.5 and source-distances of up to 200 km (Ambraseys et al. 1996, 2005). This equation allows integrating the influence of the seismogenic fault's hanging and footwall site effect in the PGA attenuation previously investigated by Abrahamson–Silva (2007), Campbell–Bozorgnia (2007), Chiou–Youngs (2007); and Houqun et al. (2016).

$$\log(PGA) = -1.39 + 0.261M_s - 0.922\log(r) + 0.5P \tag{11}$$

In this equation the coefficient r is defined by (Eq. 12).

$$r = \sqrt{d^2 + h^2)} \tag{12}$$

In which, PGA is peak ground acceleration in g. $M_s$ is the earthquake magnitude; r is the distance attenuation parameter from the hypocenter, d is the shortest distance from the station to the surface projection of the fault rupture; h is a constant best described as a representative hypocentral depth effect on acceleration, and P accounts for errors or uncertainties. The integration of ruggedness factor, PGA amplification coefficients and fictitious depth (h) in the PGA is presented below.

i. Ruggedness factor (RF)

The RF (Fig. S9 presenting the RF maps for Haiti, Taiwan, Lushan and Luding) or terrain ruggedness classifies terrain as smooth or rugged. More rugged terrain is generally associated with a higher with a higher landslide susceptibility during seismic events.

It considers the changing morphological conditions around a pixel (Gautam et al. 2021; Pyakurel et al. 2024). Often ND computed without considering the RF can become very high for pixels marked by steep slopes, while neighboring pixels do not have such high steepness. The RF helps smooth the effect of steep slopes on the ND calculated for singular pixels by considering the neighborhood of those pixels. Thus, steep slope and related low FS values computed for singular pixels may only lead to larger Newmark Displacement values if also the surrounding area is marked by a higher ruggedness of the topography. Indeed, if this is not the case, the low FS value assessed for a singular pixel within a more stable area would not lead to major instability. The RF is derived from the OpenTopography DEM of 30 m resolution using the Topographic Roughness Index tool of the QGIS 3.28.7 software. The DEM is first smoothed to 25 × 25 pixels, then the values are normalized (with a common factor for all the regions studied) to obtain values of 0–3, with 0 for plain regions and 3 for deep valleys with steep slopes.

The RF (Fig. S9 presenting the RF maps for Haiti, Taiwan, Lushan and Luding) or terrain ruggedness classifies terrain as smooth or rugged. More rugged terrain is generally associated with a higher with a higher landslide susceptibility during seismic events. It considers the changing morphological conditions around a pixel (Gautam et al. 2021; Pyakurel et al. 2024). Often ND computed without considering the RF can become very high for pixels marked by steep slopes, while neighboring pixels do not have such high steepness. The RF helps smooth the effect of steep slopes on the ND calculated for singular pixels by considering the neighborhood of those pixels. Thus, steep slope and related low FS values computed for singular pixels may only lead to larger Newmark Displacement values if also the surrounding area is marked by a higher ruggedness of the topography. Indeed, if this is not the case, the low FS value assessed for a singular pixel within a more stable area would not lead to major instability. The RF is derived from the OpenTopography DEM of 30 m resolution using the Topographic Roughness Index tool of the QGIS 3.28.7 software. The DEM is first smoothed to 25 × 25 pixels, then the values are normalized (with a common factor for all the regions studied) to obtain values of 0–3, with 0 for plain regions and 3 for deep valleys with steep slopes.

ii. PGA amplification factors: topographic smoothing operators, hanging wall/footwall coefficients, preferred slope aspect coefficients, and fictitious depth parameter (h)

To account for the acceleration, deceleration, convergence, and divergence of seismic waves as they propagate from the source through subsurface soils, adaptive smoothing operators, with values ranging from 0.7 to 1.5 (as proposed by Zevenbergen and Thorne 1987, and Moore et al. 1991), were implemented in ArcGIS 10.5. These operators previously used by Wang et al. (2018) and Djukem et al. (2024) for topographic amplification, were also used in this investigation to simulate seismic wave propagation as a function of preferred slope orientation involved by the fault focal mechanism). Similarly, Houqun et al. (2016) recommended after performing the statistical regression analysis of 154 horizontal strong earthquake records with earthquake magnitudes recorded on the bedrock in the western United States during the years 1933–1994, to the use of near-site factors for seismic motion acceleration ranging from 0 to 1.5 for a fault distance of 2.5–5 km, while computing the PGA. Therefore, considering the fault focal mechanism (strike-slip, thrust and reverse faults), different factors ranging from 1.1 to 1.5 were assigned to the footwall (FW) and hanging wall (HW) in Luding, Taiwan, Lushan and Haiti (Fig. 4). The highest factor indicates that the evaluation factor is more favorable for the development of landslides and the lowest indicates that the probability of landslide development by this evaluation factor is lower.

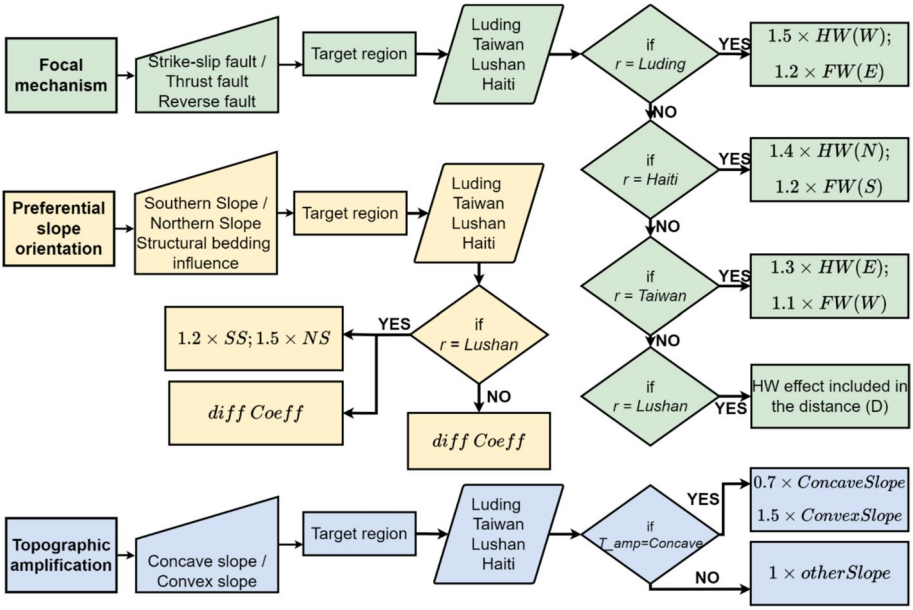


**Fig. 4** The computation flow chart of the PGA amplification coefficients: focal mechanism, preferred slope aspect, and topographic amplification. HW means hanging wall and FW means footwall. W, E, S, N, SS, and NS represent the west, east, south, north, south-south, and north–south directions

The seismogenic fault and epicentral distance maps were produced by digitizing the corresponding activated fault segments and/or epicenter points. The sources of the seismogenic faults and epicenters of the targeted seismic events are shown in the supplementary table (Table S2). The combined distances to both the epicenter and activated fault segment were computed using the Euclidean distance tool of ArcGIS 10.5. The resulting mean epicentral distance map was calculated using the ArcGIS 10.5 raster calculator. Figures S10 and S11, present the PGA maps, and amplified PGA, respectively.

In the Ambraseys' PGA attenuation law, $h$ is assimilated to a fictitious depth parameter rather different from the real focal depth of the earthquake. $h$ is typically proportional to the average depth of some type of earthquakes and also marks the focusing effect around faults: smaller values for shallower earthquake hypocenters, typically also for strike-slip faults with strong focusing of high PGA values near the fault rupture (Luding and Haiti events); larger values for high-magnitude events with fault rupturing over a wide range of depths (e.g. for Taiwan). It acts as a parameter to improve the equation's performance in estimating strong ground motions. The following PGA attenuation factors of 3, 5, 9, and 6, have been assigned to Luding, Haiti, Taiwan, and Lushan events, respectively (Fig. S12). These values were chosen to better fit the ground motion data observed over a wide range of earthquake magnitudes and distances, based on the similarity of the shape of their curves to that of the PGA attenuation curves calculated using the laws of the original Huo and Hu (1992); Ambraseys et al. (1996); adapted Bindi et al. (2017) for magnitudes from M = 5 to 6.5 (Excel sheet provided as supplementary material).

### 3.5 Assessing the predictive power of the site-adaptable ND and Jin et al. (2019) models

We compared the predictive capabilities of our models with those calculated using the equation of Jin et al. (2019). For practical application, we evaluated the efficiency of ND models computed with both equations by calculating the proportion of landslide pixels (Eq. 13), within each ND category. Jibson et al. (2000), Djukem et al. (2024), and Li et al. (2024a, b) also used this method.

$$Curvevalue = \frac{Nb\ of\ land\ slide\ pixels\ in\ ND\ classi}{Nb\ of\ pixels\ of\ ND\ classi} \times \frac{Total\ land\ slide\ pixels}{Total\ pixels\ of\ ND} \quad (13)$$

The first part of the formula indicates the likelihood of landslides occurring within that specific ND class. A higher value suggests that a large proportion of pixels in that class are associated with landslides. The second part of the formula serves to normalize values. This accounts for differences in the overall number of pixels across all classes, allowing for a more balanced comparison. First the landslide polygons were converted to raster in the ArcMap 10.6 interface. Initially, the operation failed due to a mix-up in some polygons. This was likely caused by the automatic extraction of the landslides. We checked inventories to eliminate and/or modify incorrect and unreliable polygons.

## 4 Results

### 4.1 Variation of slope displacement in each region

Jibson and Keefer (1993), Wang et al. (2014), and Cui et al. (2019) suggested that the slope displacement is initiated at ND threshold values between 5 and 10 cm. The ND models are therefore categorized into the following six classes: ND < 0.5, 0.5–2, 2–10, 10–25, 25–80, and ND ≥ 80 cm.

#### 4.1.1 Predicted displacement for Haiti 2010 and 2021 events

The final ND models for Haiti takes into account: the hanging wall effect of the Léogâne blind thrust and Enriquillo-Plantain Garden strike-slip faults; amplified curvature; roughness; wetness index; mean distance to 2010 and 2021 epicenters and activated fault segments. For the SAND models, the predicted displacements range between 0–155 cm for Haiti 2010, and 0–126 cm for Haiti 2021. High displacement values are observed both at near and far-fault sites. The ND values decrease with distance from the epicenter for Haiti 2021. Landslides are dominant in the ND classes with displacement greater than 10 cm for both Haiti 2021 and 2010 (Figs. 5 and 6). However, the J19 models predicted displacement values vary between 0 and > 500 m for both Haiti 2010 and 2021. Very high displacements (≥ 80 cm) are observed all over the target area, even very far away from the 2010 and 2021 activated fault segments. This is marked by the predominance of the red and orange colors (Fig. 6C and D).

The sites displaying high ND values are precisely areas of high probability of slope failures. The spatial distribution of the highest SAND values for the Haiti 2021 ND model, almost perfectly delineate the actual landslide areas (Fig. 5A and B). Regardless

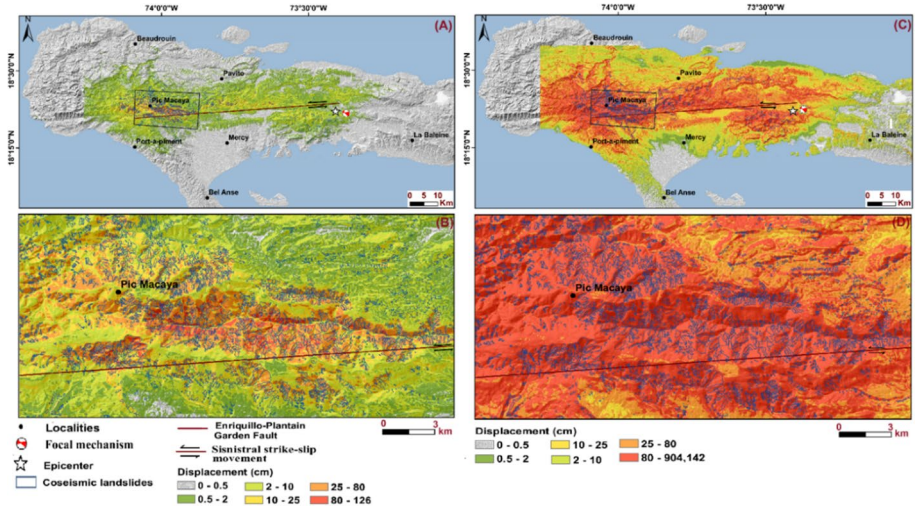


**Fig. 5** Spatial distribution of ND values and the 2021 ETLs; **A**–**B** show most of the 2021 ETLs in areas with high ND values (2 to > 80 cm) in the ND model computed with the site-adaptable approach or SAND; **C**–**D** show the ND model computed with the Jin et al. (2019) equation or J19; the Enriquillo-Plantain Garden fault activated segment is represented by the red line

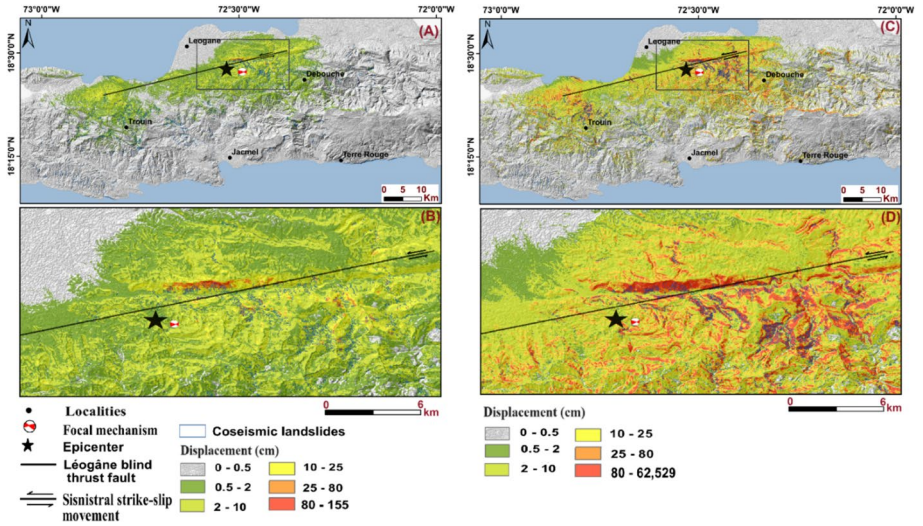


**Fig. 6** Spatial distribution of ND values and ETLs: **A** and **B** show most of the 2010 landslides in areas with low to moderate ND values (0.5–25 cm) computed with SAND; **C**–**D** show the ND model computed with J19; the Léogâne blind thrust fault activated segment is represented by the black line

of the spatial distribution of the landslides, the J19 model of Haiti 2021 and 2010 shows ND ≥ 10 cm throughout the area. Considering Haiti 2010, landslides are also observed in areas with both low and high ND values (Fig. 6B and D) for both the SAND and J19 models. High displacement values are also observed far from the epicenter and the activated fault, in areas without landslides. However, for the SAND models, high displacements

appear more concentrated near the first 10 km of the activated fault trace (Fig. 6B), while for the J19 models (Fig. 6D), very high displacements are observed throughout the area.

### 4.1.2 Spatial distribution of ND and ETLs in Taiwan

The 1999 Chi Chi earthquake ND model considers the hanging wall effect of the thrust Chelungpu fault, along with the wetness coefficient; slope aspect; amplified curvature; roughness; and mean distance to the source (epicenters and fault). The predicted displacements range from 0 to 108 cm for SAND, and 0 to ≥ 500 cm for J19. For SAND, the low ND values (0- 0.5 cm) are dominant on the eastern side of the Chelungpu fault, representing the footwall. This is also consistent with the absence of landslides. ND values ≥ 0.5 cm and landslides are dominant on the western side of the fault or hanging wall (Fig. 7A, B). The ND values decrease less rapidly with distance from the epicenter on the hanging wall. Landslides are once dominant in the ND classes with displacement greater than 10 cm. However, landslides are observed in areas with both low (gray, green, and light green) and high (yellow, orange, and red) ND values (Fig. 7B). However, similar to Haiti, the J19 models show very large displacements (≥ 80 cm) throughout the target area, even far from the activated fault segment, both on the hanging wall and the footwall. (Fig. 7C-D). Regardless of the spatial distribution of the landslides, the J19 model of Taiwan 1999 shows ND ≥ 10 cm throughout the area.

### 4.1.3 Spatial distribution of ND and ETLs for Lushan 2013 and 2022 events

The Lushan 2013 and 2022 slope displacement models include the corresponding focal mechanism effects, curvature, roughness, wetness coefficient, and mean epicentral distance for the 2013 earthquake, but only the distance to the 2022 event epicenter. The displacement values fluctuate between 0 and 103 cm for Lushan 2013 for SAND, and from 0 to ≥ 500 cm for J19. The low SAND values (≤ 0.5 cm) are mostly observed on the eastern side of the Longmenshan fault zone, representing the footwall, where there are no landslides. SAND values ≥ 0.5 cm and landslides are dominant on the western side of the fault or hanging wall (Fig. 8B and D). On the hanging wall, the ND values decrease less rapidly as the distance from the activated fault and the epicenter increases, like Taiwan 1999.

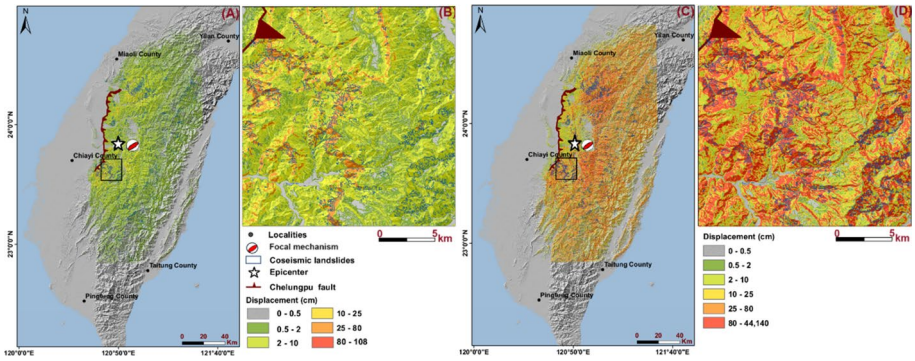


**Fig. 7** Spatial distribution of ND values and ETLs for 1999 Chi Chi earthquake in Taiwan. computed with SAND (**A**–**B**); **C**–**D** show the ND model computed with J19. The enlarged parts of the image (**B** and **D**) show most landslides in areas with ND ≥ 2 cm on the hanging wall for SAND and J19

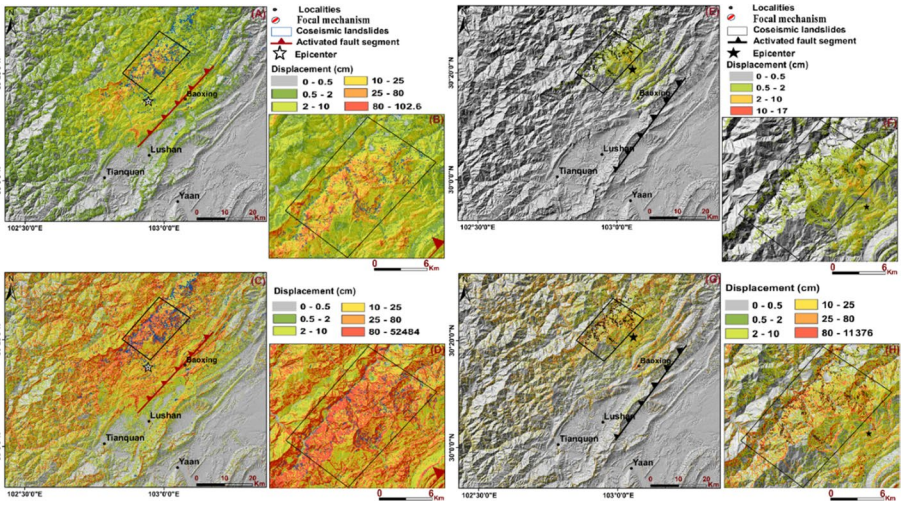


**Fig. 8** Spatial distribution of ND values and ETLs for Lushan 2013 (**A**, **B**, **C**, **D**) and 2022 (**E**, **F**, **G**, **H**) earthquakes. The distribution of these landslides in areas with both low and moderate ND values for SAND (**A**, **B**, **E** and **F**), and for J19 (**C**, **D**, **G**, and **H**), is observed in the magnified parts of the pictures (**B**, **F**, **D** and **H**)

As in Haiti and Taiwan, the predicted displacements of the J19 models for Lushan 2013 vary from 0 to > 500 m, and very high displacements (≥ 80 cm) are observed throughout the target area, even far away from the activated fault segment (Fig. 8C, D). The J19 model of Lushan 2013 is dominated by ND ≥ 10 cm throughout the region, whether on the hanging wall or the footwall, regardless of the spatial distribution of the landslide. For the Lushan 2022 event with the lowest magnitude of Mw5.9, the predicted displacements vary between 0 and 17 cm for SAND, and from 0 to ≥ 500 cm for J19. However, landslides once predominate in the ND categories with displacements greater than 10 cm using both equations. A similar landslide-displacement distribution was also the case in Taiwan and Haiti.

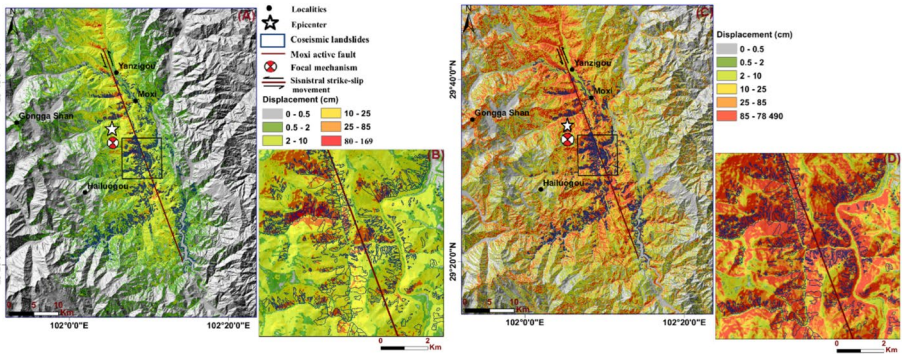


**Fig. 9** Spatial distribution of ND values and ETLs for the Luding 2022 earthquake. Landslides are predominant in areas with ND values ≥ 2 cm for SAND (**A**-**B**) as indicated by the light green, yellow, orange, and red colors in the enlarged parts of the image. For J19 landslides are predominant in areas with ND values and ≥ 10 cm for J19 (**C**-**D**)

#### 4.1.4 Spatial distribution of ND and ETLs in Luding

The computed ND models take into account the left strike-slip mechanism of the Moxi fault segment; preferred slope orientation, amplified curvature; roughness; wetness index; and mean distance to the epicenter of the source. The predicted displacements range from 0 to 169 cm for SAND (Fig. 9A, B), and from 0 to ≥ 500 cm for J19 (Fig. 9C, D). The ND values also decrease with distance from the fault and epicenter for SAND. Very high ND values (≥ 80 cm), indicated by the red color (Fig. 9A, B), are mostly observed on the western side of the left-lateral strike-slip Moxi fault segment. The distance over which displacements greater than 0.5 cm extend is greater on the west side of the fault (Fig. 9B). There are also a few areas of high ND without landslides, and areas of low ND with landslides. Landslides are dominant in the ND classes on the western side of the activated fault, with displacement greater than 10 cm for Luding 2022.

Similarly, for Haiti, Taiwan, and Lushan, displacement values ≥ 80 cm are observed throughout the Luding area on both sides of the activated fault segment (Fig. 9D). The J19 model of Luding 2022 shows ND ≥ 10 cm throughout the area, regardless of the focal mechanism effect, the spatial distribution of landslides, and the preferred slope orientation.

### 4.2 Predictive power of the SAND and J19 models in Haiti, Taiwan, Lushan and Luding

First, we present in Fig. 10A a general overview of the ETL prediction by comparing the total surface area (TSA) of landslides triggered by each of the analyzed earthquake events with the TSA of NDs larger than the common threshold of 2 cm computed by the two methods, SAND, and J19. The first are marked by green bars in Fig. 10A, the second, respectively by blue and red bars. This graph shows that logically the TSA for landslides roughly augments with increasing magnitude; the only exception is the Mw = 7.0 Haiti 2010 event that triggered more than 20,000 landslides, but all being relatively small, and thus the related TSA is also smaller than the one observed for the Mw = 6.8 Luding event. The main reason is that the latter occurred in the middle of a mountain region, while the Haiti 2010 event occurred close to the sea and mostly affected hilly areas – a fact that had already been outlined by Havenith et al. (2022). Globally, the TSA of NDs larger than 2 cm computed by each of the two methods for the six events follow the same trend. Related TSA are however much larger, typically 50 to 100 times larger for the J19 method and about 6–50 times for SAND. This marks also the fact that for most events the 2 cm threshold is probably too low, especially for the J19 method that systematically produces larger NDs than SAND as could already be observed from the maps presented above. Furthermore, below we will show that the landslide predictions provided in terms of ND calculations made with SAND are more specifically highlighting zones that were indeed affected by landslides during the respective events, also for larger ND classes.

For the presentation of related statistical results, the ND models are categorized into the following 7 classes: ND < 0.012, 0.012–0.25, 0.25–1.2, 1.2–6, 6–16, 16–50 and 50–150 cm.

Figure 10B presents for both models the ratios of TSA of landslides per ND class normalized by the TSA of all landslides divided by the TSA of the respective class normalized by the TSA of the all ND classes; in Fig. 10B related results are shown for the two events in Haiti (2010 and 2021), in Fig. 10C those for the two Lushan events (2013 and 2013) and in Fig. 10D those for the 2022 Luding and for the 1999 Taiwan earthquakes.

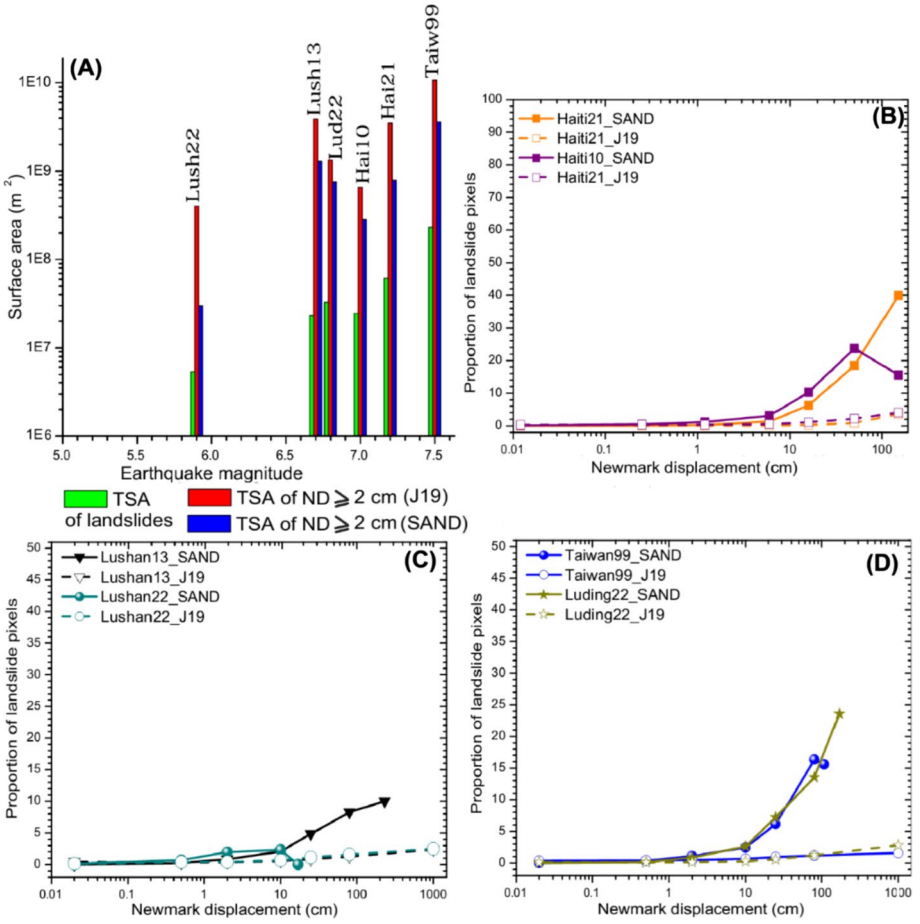


**Fig. 10** **A** Comparison of total surface areas (TSA) of landslides (green bars) triggered by each of the analyzed earthquake events (for increasing magnitudes, from left to right: Mw = 5.9 Lushan 2022–Lush22, Mw = 6.7 Lushan 2013 – Lush13, Mw = 6.8 Luding 2022 – Lud22, Mw = 7.0 Haiti 2010–Hai10, Mw = 7.2 Haiti 2021–Hai21, Mw = 7.5 Taiwan 1999 – Tai99) with the TSA of NDs larger than 2 cm calculated for the respective event by using the SAND (blue bars) and the J19 (red bars) methods. (**B**, **C**, **D**) SAND and J19 predictive power curves: **A**, **B**, **C** proportion of landslide pixels normalized to the sum of all classes within each displacement category for the Haiti, Taiwan, Lushan and Luding earthquake-induced landslides. The curves from the SAND model are shown as solid lines, and the curves plotted with the J19 results are shown as dashed lines

All these graphs show that for both models (solid lines for SAND and dashed lines for J19), with increasing displacement, the proportion of landslides within each ND class increases almost gradually, except for the largest ND values computed by SAND for the Haiti 2010 event. In general, however, per ND class the proportion of landslides is clearly higher for SAND than for the J19 model, which is likely because J19 produces related ND values for much wider areas, which reduces the 'density' of predicted landslides in those areas. SAND thus appears as a more efficient model as more landslides

are clustered within smaller areas of medium to high ND value classes (according to a type of efficiency as highlighted by Li et al. 2024a, b).

More specifically, slope failures appear to start when SAND values fluctuate between 2 and 10 cm in Haiti, Taiwan, Lushan, and Luding (Fig. 10B-D, Tables S3 and S4); while those threshold values are typically higher for the J19 model. The lower threshold value of 2 cm is in accordance with the results obtained in the Betic Cordillera mountainous zones by Rodríguez et al. (2014), and slightly different from the 5 to 10 cm suggested by Jibson and Keefer (1993) and Cui et al. (2019), which would fit better for the J19 model.

It is also important to note that the Lushan 2022 event yields the lowest ND values with 17 cm as maximum displacement (Fig. 10), which is due to the lower magnitude of the earthquake.

## 5 Discussion or integration of results

In this section, we discuss various factors that affect the SAND and J19 methods effectiveness in each region, including seismotectonic activity, model parameters, landslide specific features, hydrogeological, and geological conditions.

### 5.1 Factors differentiating Haiti, Taiwan, Lushan and Luding earthquake events: influence on the ND

The maximum SAND values obtained can be classified from highest to lowest as follows: Mw = 6.7 Lushan 2013 (209 cm); Mw = 6.8 Luding (169 cm); Mw = 7.0 Haiti 2010 (155 cm); Mw = 7.2 Haiti 2021 (126 cm); Mw = 7.5 Taiwan 1999 (108 cm) and Mw = 5.9 Lushan 2022 (17 cm). For J19, the maximum NDs values in these regions are even higher (> 500 cm).

The predicted SAND efficiency assessment shows that 33 to 85% of landslides inventoried during Haiti (2010 and 2022), Lushan 2013, Luding 2022 and Taiwan 1999, occurred in areas with a high probability of slope failure considering both the displacement thresholds of 2 cm (Table 2). For Lushan 2022, only 8% of the landslides were captured by the SAND model using the same thresholds. This can be mainly explained by the

**Table 2** Proportion of landslides predicted per region by the SAND and J19 models, considering 2 cm as thresholds

| Models | Haiti 2021 | Haiti 2010 | Lushan 2013 | Lushan 2022 | New Lushan 2022 | Taiwan 1999 | Luding 2022 | Luding 2022 |
|---|---|---|---|---|---|---|---|---|
| *Cumulative proportion (in %) of landslides for ND classes > = 2 cm, normalized with respect to total number of landslides* | | | | | | | | |
| SAND | 91 | 45 | 70 | 8 | 87 | 56 | 80 | 80 |
| J19 | 99 | 92 | 94 | 91 | 91 | 93 | 91 | 91 |
| *Cumulative proportion (in %) of landslides normalized with respect to size of region marked by ND > = 2 cm* | | | | | | | | |
| SAND | 12 | 15 | 3 | 2 | 2 | 3 | 11 | 11 |
| J19 | 1 | 2 | 1 | 0 | 0 | 1 | 1 | 1 |

lower magnitude (Mw 5.9) of this earthquake, which was not sufficient to generate strong motions. The landslides, despite the earthquake's weak magnitude, could be due to slope material weakened by the 2008 Wenchuan and 2013 Lushan earthquakes, and the heavy rainfall recorded around the 2022 event (Du et al. 2023; Tang et al. 2023). Each of these regions also has some specific features that could affect the predictive capabilities of ND models as highlighted below.

The SAND threshold displacement from 0 to 10 cm plays a crucial role in shaping landslide risk management strategies by informing key decision-making areas:

1. Risk assessment and early warning: the threshold helps define criteria for triggering alerts, supporting timely evacuation and protective measures in high-risk zones.
2. Resource prioritization: areas with higher predicted displacements can be prioritized for inspection and mitigation efforts, ensuring efficient allocation of resources.
3. Engineering considerations: understanding expected displacement aids in designing mitigation structures, such as retaining walls and drainage systems, to enhance slope stability.
4. Long-term monitoring and adaptation: continuous assessment of threshold variability supports improvements in predictive models and adaptive risk management strategies.

While SAND offers a useful tool for landslide risk management, its application should be complemented with field observations and additional geotechnical analyses to ensure robust decision-making.

#### 5.1.1 Influence of the seismic related factors: pre-event seismicity, focal mechanism, fault geometry, and aftershocks on slope displacement

During earthquakes landslides occur more often in rocks or sediments weakened by previous climatic or seismic events and in the neighborhood of wide fault zones. For instance, the 2013 and 2022 Lushan earthquakes occurred only several tens of kilometers in the southwest of the epicenter of the Wenchuan earthquake, in an area where continuous strong earthquakes have weakened the solid-rock materials of the slopes. These materials presented loose and fractured structures with a high probability of landslide occurrence prior to the 2013 earthquake, as highlighted by Du et al. (2023). In addition, the 2022 Lushan Mw 5.9 earthquake occurred in the aftershock zone of the 2013 Lushan and the 2008 Mw = 7.9 Wenchuan earthquakes, causing more landslides than expected (Chen et al. 2013; Gao et al. 2014; Tang et al. 2023). The presence or absence of a surface rupture along the activated fault also affects slope failures. Surface ruptures often coincide with areas of stronger shaking, which can increase the likelihood of landslides. However, this is not always the case. In some instances, shaking intensity near a surface rupture may be lower, as seen near a 10-m-high scarp that appeared during the 2008 Wenchuan earthquake in Beichuan, where a nearby house experienced relatively mild shaking despite its proximity to the rupture. The energy released by a fault rupture increases the pressure on nearby faults, which can lead to future earthquakes of varying magnitudes (Richardson and Marone 2008; Dong and Luo 2022). Among the studied events, the Mw = 6.8 Luding 2022 and the Mw = 7.5 Taiwan 1999 earthquake generated the largest surface ruptures, of several tens of kilometers of length. Highest landslide densities could thus be observed near surface

ruptures (see e.g. the 2022 Luding event) or outcrops of activated fault segments (Haiti 2021 event) that are in mountain regions. The Lushan and Taiwan earthquakes further confirm that higher landslide densities are observed in the hanging wall parts of activated thrust faults, as previously outlined for the 2008 Wenchuan earthquake (Gorum et al. 2011; Fan et al. 2018).

### 5.1.2 Influence of model parameters and specific landslide features

The parameters used to design ND models determine their ability to predict slope failures. The SAND models computed in this work are suitable for the prediction of shallow slides with a depth of 5 m. The proportion of landslides was found to increase with ND values in Haiti, Lushan, Luding, and Taiwan. Moreover, in the Luding region, the highest proportion of landslides (22%) occurred in the class with the highest ND ≥ 80 cm. This percentage is significantly higher than the 19% and 3% predicted by the best ND scenarios for shallow landslides previously calculated by Djukem et al. (2024). These authors used the equations developed by Miles and Ho (1999) and Jin et al. (2018) incorporating topographic and slope orientation amplifications in their analysis (Fig. 11A).

The spatial distribution pattern of ETLs is also of great importance as highlighted by Djukem et al. (2024). The Luding 2022 triggered mostly shallow, small-sized, and high-altitude initiation landslides (1000–2500 m). The initiation of movement or detachment zone, whether from the summits or mid-slopes, has an impact on the effectiveness of the ND models. ETLs triggered in Haiti, Taiwan, Lushan and Luding presented different patterns. The Luding landslides were predominantly found on steep slopes of 30°–50°. They were also preferentially distributed in the E-, SE-, and S-facing slopes as pointed out by (Djukem et al. 2024). These landslides were mainly located in the southeastern area of the epicenter (Dai et al. 2023; Guo et al. 2024).

The 2022 Lushan earthquake triggered mostly shallow, disrupted landslides and rock falls, at higher elevations (1000–1600 m) and steeper slopes (30°–50°) than the landslides triggered by the 2008 Wenchuan and 2013 Lushan earthquakes (Zhao et al. 2022). These landslides appear to be initiated in high-altitude and steep-slope areas. The clustering of small landslides on the ridges indicates the seismic amplification effects (Shao et al. 2022a).

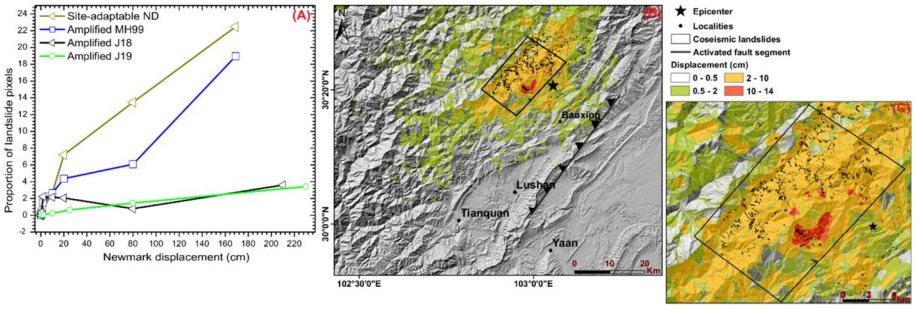


**Fig. 11** **A** Predictive power of models obtained with SAND, Jin et al. (2019), and previous ND models computed by Djukem et al. (2024) using the Miles and Ho (1999) and Jin et al. (2018) equations to predict the 2022 Luding ETLs. **B** New ND model for Lushan 2022 computed using SAND, but reducing the FS in all areas affected by the 2013 Lushan earthquake

Moreover, the flexibility of the SAND approach allows to improve the prediction of the 2022 Lushan from 8% to > 80% in cumulative > = 2 cm. This improvement was achieved by incorporating the focal mechanism for calculating the PGA (as many landslides occurred quite far from the epicenter on the hanging wall side) and reducing the FS in all areas affected by the 2013 Lushan earthquake (see the New Lushan 2022 in Table 2 and Fig. 11B).

#### 5.1.3 Influence of hydrogeological conditions

The climate through dry and wet seasons, and extreme meteorological events such as typhoons, hurricanes influence the hydrogeological conditions of the sites and consequently the water content of the materials (Lin et al. 2008; Chen and Hawkins 2009). These conditions are determinant for the types, sizes, and even the initiation zones of coseismic landslides.

Likewise, the effect of the 2010 Haiti earthquake may also have been slightly increased due to some climatic forcing such as the 2004 tropical storm Jeanne and nearby 2008 hurricanes (Fay, Gustav, Hanna, and Ike) as mentioned by Gorum et al. (2013). Still, compared to the 2010 earthquake, even much larger landslides were triggered by the 2021 Haiti earthquake within a wider area. The more extensive 2021 landslide activity could be explained by the larger magnitude of the event and by the impacts of recent hurricanes that had directly crossed the epicentral region of the 2021 event: 'Matthew' in October 2016 and 'Grace' just two days after the main shock (Calais et al. 2022; Havenith et al. 2022). Similarly, Chen and Hawkins (2009) also concluded from their study of the 1999 Chi-Chi ETLs that typhoon Herb (1996) may almost have doubled the surface area of landslides caused by the earthquake.

Moreover, on May 6, 2022, Lushan, located in Ya'an City, experienced continuous rainfall, reaching a cumulative value of 330 mm on June 5. In addition, 3 min after this earthquake, Baoxing County in the same city experienced a second earthquake with a magnitude of 4.5 (Du et al. 2023). These factors may have amplified the effects of the Lushan Mw 5.9 earthquake on June 1.

### 5.2 Limitations of existing ND and SAND models

#### 5.2.1 Limitations of existing ND equations

Existing ND equations mainly rely on seismic and geotechnical parameters like PGA and $A_c$, often neglecting key factors such as fault rupture type, directivity effects, and seismogenic zone depth (Wang et al. 2014). Many models, including J18, fail to account for $I_A$ attenuation with distance, overemphasizing slope stability and leading to overestimated ND values in distant regions where landslides do not occur (Djukem et al. 2024). This results in poor spatial predictions, particularly for earthquakes with concentrated landslides near the epicenter, such as the Luding earthquake. Additionally, ND models often overlook topographic amplification and hydrological influences, which can intensify ground shaking or weaken soil stability (Chen and Hawkins 2009; Gorum et al. 2013; Havenith et al. 2022). Their reliability is further impacted by incomplete landslide inventories due to remote sensing limitations, survey constraints, and inconsistent documentation, leading to biased statistical correlations and inconsistent coefficients (Hussain et al. 2023).

Moreover, most ND equations lack a mechanistic basis, limiting their applicability across diverse environments. Models developed in humid, tectonically active regions like Taiwan and Japan may not hold in arid areas like Iran and North Africa (Notti et al. 2023). Similarly, equations calibrated for moderate-magnitude earthquakes (Mw 5.5–6.5) may fail for larger events (Mw > 7), where different triggering mechanisms dominate. Without a solid physical framework, these ND equations often struggle to generalize beyond the specific datasets.

### 5.2.2 Limitations of the SAND models

As with many other predictive models, the reliability of the site-adaptive ND model is highly dependent on the quality of the data available for computation and the landslide catalog used for validation. The geomechanical data used in this study are averages from literature rather than from laboratory experiments. Therefore, there may be uncertainties in the predicted slope displacement. Also, automatic extraction by remote sensing can compromise the quality of landslide catalogs used for the validation as previously noticed by Xu et al. (2014); Marc and Hovius (2015); and Valagussa et al. (2019). In addition, except for Luding, the site-adaptable ND and J19 models developed for Haiti, Lushan and Taiwan are not easily comparable to existing models because previous models were often focused only a small portion of the areas affected by ETLs. Furthermore, previous ND models implemented in Haiti, Taiwan, and Lushan used empirical equations and/or different geomechanical and geoenvironmental factors (Wang and Lin 2010; Yuan et al. 2016; Jin et al. 2018). Also, the assumption of a quadratic relationship between ND and PGA, and a non-linear relationship between ND and $A_c$ may lead to some misrepresentation, as different regions may exhibit more complex responses to seismic inputs. Therefore, for future work, we will consider refining the SAND approach based on larger and more diverse datasets. Moreover, a comprehensive sensitivity analysis of SAND parameters will be carried out to quantify the influence of key input variables, such as PGA and $A_c$, on ND predictions. This will enhance the model's reliability and applicability across diverse seismic and geoenvironmental conditions.

## 6 Conclusions

At present, there is no universally recognized ND equation for predicting ETLs on a regional scale. We examine the effectiveness of ND models in different tectonic environments and identify why certain values of the ND equation coefficients work better in some places than in others. The affected regions in Haiti, Taiwan, Luding, and Lushan present different geological, geomorphological, seismotectonic, and structural characteristics that have not been considered in previous ND models. Moreover, the ND equations obtained by statistical regression on data from several seismic stations only provides a general overview. They are not sufficient for a detailed understanding of the interactions between seismic waves and the specific conditions of individual sites. We propose a site-adaptable ND approach (SAND) accounting for region- and site-specific factors including seismotectonic and climatic conditions, soil-rock properties, hydrogeology, topography, as well as pre-event slope weakening, to predict shallow landslide displacements across various tectonic environments. The predictive power of the resulting SAND models was compared with

that of the statistically derived ND based on PGA proposed by Jin et al. (2019). The SAND models showed higher predictive performance than the J19 models in Haiti, Lushan, Luding, and Taiwan. The J19 equation, which is considered representative of the statistically derived ND equations, may require additional calibration or adaptation for specific tectonic environments. This study suggests that the varying effectiveness of ND equations across regions is likely due to previously unconsidered factors that are unique for each area, particularly changes in pre-event conditions. The advantage of this method compared to other classical statistical methods is that this process-based technique allows us to make those predictions without any calibration by a landslide inventory, which is typically not available before several weeks after the main shock.

**Supplementary Information** The online version contains supplementary material available at https://doi.org/10.1007/s11069-025-07200-8.

**Author contributions** Danny Love Wamba Djukem: Conceptualization, data curation, formal analysis, investigation, methodology, validation, visualization, roles/writing—original draft, writing—review and editing. Xuanmei Fan: Conceptualization, data curation, formal analysis, funding acquisition, investigation, project administration, resources, software, supervision, validation, roles/writing—original draft, writing—review and editing. Hans-Balder Havenith: Conceptualization, data curation, formal analysis, investigation, methodology, project administration, resources, software, supervision, validation, visualization, roles/writing—original draft, writing—review and editing.

**Funding** This research is financially supported by the National Science Fund for Distinguished Young Scholars of China (Grant 42125702), the Natural Science Foundation of Sichuan Province (Grant 22NSFSC0029), the Tencent Foundation through the XPLORER PRIZE (Grant XPLORER-2022–1012).

**Data availability** All data can be provided by the corresponding author upon request.

## Declarations

**Competing interests** The authors declare no competing interests related to the submitted work.

## References

Abrahamson NA, Silva WJ (2007) NGA ground motion relations for the geometric mean horizontal component of peak and spectral ground motion parameters. Pacific Earthquake Engineering Research Center, University of California, Berkeley, pp. 1–378

Allen CR, Zhuoli L, Hong Q, Xueze W, Huawei Z, Weishi H (1991) Field study of a highly active fault zone: the Xianshuihe fault of southwestern China. Geol Soc Am Bull 103(9):1178–1199. https://doi.org/10.1130/0016-7606(1991)103%3c1178:fsoaha%3e2.3.co;2

Amatya P, Scheip C, Déprez A et al (2023) Learnings from rapid response efforts to remotely detect landslides triggered by the August 2021 Nippes earthquake and Tropical Storm Grace in Haiti. Nat Hazards 118:2337–2375. https://doi.org/10.1007/s11069-023-06096-6

Ambraseys NN, Simpson KA, Bommer JJ (1996) Prediction of horizontal response spectra in Europe. Earthq Eng Struct Dyn 25(4):371–400

Ambraseys NN, Douglas J, Sarma SK et al (2005) Equations for the estimation of strong ground motions from shallow crustal earthquakes using data from Europe and the Middle East: horizontal peak ground acceleration and spectral acceleration. Bull Earthq Eng 3:1–53. https://doi.org/10.1007/s10518-005-0183-0

An Y, Wang D, Ma Q, Yueren X, Li Y, Zhang Y, Liu Z, Huang C, Jinrong S, Li J, Li M, Chen W, Wan Z, Kang D, Wang B (2023) Preliminary report of the September 5, 2022 MS 6.8 Luding earthquake, Sichuan, China. Earthq Res Adv 3(1):100184. https://doi.org/10.1016/j.eqrea.2022.100184

Badola S, Mishra VN, Parkash S, Pandey M (2023) Rule-based fuzzy inference system for landslide susceptibility mapping along national highway 7 in Garhwal Himalayas India. Quater Sci Adv 11:100093. https://doi.org/10.1016/j.qsa.2023.100093

Bai M, Chevalier ML, Pan J, Replumaz A, Leloup PH, Métois M, Li H (2018) Southeastward increase of the late Quaternary slip-rate of the Xianshuihe fault, eastern Tibet. Geodynamic and seismic hazard implications. Earth Planet Sci Lett 485:19–31. https://doi.org/10.1016/j.epsl.2017.12.045

Bakun WH, Flores CH, ten Brink US (2012) Significant earthquakes on the Enriquillo Fault System, Hispaniola, 1500–2010: implications for seismic hazard. Bull Seismol Soc Am 102:18–30. https://doi.org/10.1785/0120110077

Bilham R (2010) Lessons from the Haiti earthquake. Nature 463:878–879. https://doi.org/10.1038/463878a

Bindi D, Cotton F, Kotha SR, Bosse C, Stromeyer D, Grünthal G (2017) Application-driven ground motion prediction equation for seismic hazard assessments in non-cratonic moderate-seismicity areas. J Seismology 21:1201–1218. https://doi.org/10.1007/s10950-017-9661-5

Boore DM, Atkinson GM (2008) Ground-motion prediction equations for the average horizontal component of PGA, PGV, and 5%-damped PSA at spectral periods between 0.01s and 10.0s. Earthq Spectra 24:99–138. https://doi.org/10.1193/1.2830434

Calais E, Freed A, Mattioli G, Amelung F, Jónsson S, Jansma P, Hong S-H, Dixon T, Prépetit C, Momplaisir R (2010) Transpressional rupture of an unmapped fault during the 2010 Haiti Earthquake. Nat Geosci 3:794–799. https://doi.org/10.1038/ngeo992

Calais E, Symithe S, Monfret T, Delouis B, Lomax A, Courboulex F, Ampuero JP, Lara PE, Bletery Q, Chèze J, Peix F, Deschamps A et al (2022) Citizen seismology helps decipher the 2021 Haiti earthquake. Science 376:283–287. https://doi.org/10.1126/science.abn1045

Campbell KW, Bozorgnia Y (2007) Campbell-Bozorgnia NGA Ground Motion Relations for the Geometric Mean Horizontal Component of Peak and Spectral Ground Motion Parameters. Pacific Earthquake Engineering Research Center University of California, Berkeley, pp 1–204

Carey JM, Massey CI, Lyndsell B, Petley DN (2019) Displacement mechanisms of slow-moving landslides in response to changes in porewater pressure and dynamic stress. Earthq Surface Dyn. 7:707–722

Chen Y-C, Chen C-Y (2024) Estimating landslide trigger factors using distributed lag nonlinear models. Environ Model Softw 185:106259. https://doi.org/10.1016/j.envsoft.2024.106259

Chen H, Hawkins AB (2009) Relationship between earthquake disturbance, tropical rainstorms and debris movement: an overview from Taiwan. Bull Eng Geol Environ 68:161–186. https://doi.org/10.1007/s10064-009-0209-y

Chen XL, Ran HL, Yang WT (2012) Evaluation of factors controlling large earthquake-induced landslides by the Wenchuan earthquake. Nat Hazards Earth Syst Sci 12(12):3645–3657

Chen XL, Yu L, Wang MM, Li JY (2013) Brief communication: landslides triggered by the Ms7.0 Lushan earthquake, China. Nat Hazards Earth Syst Sci Discuss 1:3891–3918

Chen X, Liu C, Wang M (2019) A method for quick assessment of earthquake-triggered landslide hazards: a case study of the Mw6. 1 2014 Ludian, China earthquake. Bullet Eng Geole Environ 78:2449–2458

Chen L, Mei L, Zeng B, Yin K, Shrestha DP, Du J (2020) failure probability assessment of landslides triggered by earthquakes and rainfall: a case study in Yadong codent Tibet, China. Sci Rep 10:16531. https://doi.org/10.1038/s41598-020-73727-4

Chen Z, Huang D, Wang G (2023) A regional scale coseismic landslide analysis framework: integrating physics-based simulation with flexible sliding analysis. Eng Geol 315:107040. https://doi.org/10.1016/j.enggeo.2023.107040

Chiou BSJ, Youngs RR (2007) Chiou and Youngs PEER-NGA empirical ground motion model for the average horizontal component of peak acceleration and pseudo-spectral acceleration for spectral periods of 0.01 to 10 seconds. Pacific earthquake Engineering Research Center University of California, Berkeley, pp. 1–219.

Chiou BS, Youngs RR (2008) An NGA model for the average horizontal component of peak ground motion and response spectra. Earthq Spectra 24:173–215. https://doi.org/10.1193/1.2894832

Chuang RY, Lu CH, Yang CJ, Lin YS, Lee TY (2020) Coseismic uplift of the 1999 Mw 7.6 Chi-Chi earthquake and implication to topographic change in frontal mountain belts. Geophys Res Lett. https://doi.org/10.1029/2020GL088947

Cui Y, Liu A, Chong X, Zheng J (2019) A modified Newmark method for calculating permanent displacement of seismic slope considering dynamic critical acceleration. Adv Civ Eng. https://doi.org/10.1155/2019/9782515

Dadson SJ, Hovius N, Chen H, Dade WB, Lin JC, Hsu ML, Lin CW, Horng MJ, Tien TC, Milliman J, Stark CP (2004) Earthquake-triggered increase in sediment delivery from an active mountain belt. Geology 32:733–736. https://doi.org/10.1130/G20639.1

Dai FC, Lee CF (2003) A spatiotemporal probabilistic modelling of storm-induced shallow landsliding using aerial photographs and logistic regression. Earth Surf Process Landf 28:527–545. https://doi.org/10.1002/esp.456

Dai L, Fan X, Wang X et al (2023) Coseismic landslides triggered by the 2022 Luding Ms6.8 earthquake. China Landslides 20:1277–1292. https://doi.org/10.1007/s10346-023-02061-3

Day SM, Yu G, Wald DJ (1998) Dynamic stress changes during earthquake rupture. Bull Seismol Soc Am 88:512–522. https://doi.org/10.1785/BSSA0880020512

DesRoches R, Comerio M, Eberhard M, Mooney W, Rix GJ (2011) Overview of the 2010 Haiti Earthquake. Earthq Spectra 27(1_suppl1):1–21. https://doi.org/10.1193/1.3630129

Djukem WDL, Braun A, Wouatong ASL, Guedjeo C, Dohmen K, Wotchoko P, Fernandez-Steeger TM, Havenith H-B (2020) Effect of Soil Geomechanical properties and geo-environmental factors on landslide predisposition at Mount Oku, Cameroon. Int J Environ Res Public Health 17(18):6795. https://doi.org/10.3390/ijerph17186795

Djukem WDL, Fan X, Braun A, Chevalier M-L, Wang X, Dai L, Fang C, Zhang X, Gorum T, Xu Q, Havenith H-B (2024) Traditional and modified Newmark displacement methods after the 2022 Ms 6.8 Luding earthquake (Eastern Tibetan Plateau). Landslides 21:807–828. https://doi.org/10.1007/s10346-023-02194-5

Dong L, Luo Q (2022) Investigations and new insights on earthquake mechanics from fault slip experiments. Earth Sci Rev 228:104019. https://doi.org/10.1016/j.earscirev.2022.104019

dos Santos VRN, Porsani JL (2011) Comparing performance of instrumental drift correction by linear and quadratic adjusting in inductive electromagnetic data. J Appl Geophys 73(1):1–7

Du W, Wang G (2016) A one-step Newmark displacement model for probabilistic seismic slope displacement hazard analysis. Eng Geol 205:12–23. https://doi.org/10.1016/j.enggeo.2016.02.011

Du W, Huang D, Wang G (2018) Quantification of model uncertainty and variability in Newmark displacement analysis. Soil Dyn Earthq Eng 109:286–298

Du W, Wu K, Fu X et al (2023) Failure history, mechanism, and recent run-out reproduction of the Xinhua Village landslide triggered by the 2022 Ms 6.1 Lushan earthquake. Landslides 20:2675–2693. https://doi.org/10.1007/s10346-023-02148-x

Duan HR, Chen JY, Zhang S, Xiao Long W, Chu ZM (2022) Coseismic fault slip inversion of the 2013 Lushan Ms 7.0 earthquake based on the triangular dislocation model. Sci Rep. https://doi.org/10.1038/s41598-022-07458-z

Fan X, Juang CH, Wasowski J, Huang R, Xu Q, Scaringi G, van Westen CJ, Havenith H-B (2018) What we have learned from the 2008 Wenchuan Earthquake and its aftermath: a decade of research and challenges. Eng Geol 241:25–32. https://doi.org/10.1016/j.enggeo.2018.05.004

Fan X, Fang C, Dai L et al (2022) Near real time prediction of spatial distribution probability of earthquake-induced landslides-Take the Lushan Earthquake on June 1, 2022 as an example. J Eng Geol 30(3):729–739

Gao Y, Wang Q, Zhao B, Shi YT (2014) A rupture blank zone in middle south part of Longmenshan Faults: effect after Lushan M s7.0 earthquake of 20 April 2013 in Sichuan. China Sci China Earth Sci 57:2036–2044. https://doi.org/10.1007/s11430-014-4827-2

Gautam P, Kubota T, Aditian A (2021) Evaluating underlying causative factors for earthquake-induced landslides and landslide susceptibility mapping in Upper Indrawati Watershed. Nepal Geoenviron Disast 8:30. https://doi.org/10.1186/s40677-021-00200-3

Gong W, Zekkos D, Clark M (2023) A pseudo-3D methodology for regional-scale back-analysis of earthquake-induced landslides. Eng Geol 325:107277. https://doi.org/10.1016/j.enggeo.2023.107277

Gorum T, Fan X, van Westen CJ, Huang RQ, Xu Q, Tang C, Wang G (2011) Distribution pattern of earthquake-induced landslides triggered by the 12 May 2008 Wenchuan earthquake. Geomorphology 133(3–4):152–167. https://doi.org/10.1016/j.geomorph.2010.12.03

Gorum T, van Westen CJ, Korup O, van der Meijde M, Fan X, van der Meer FD (2013) Complex rupture mechanism and topography control symmetry of mass wasting pattern, 2010 Haiti earthquake. Geomorphology 184:127–138. https://doi.org/10.1016/j.geomorph.2012.11.027

Guo C, Li C, Yang Z, Ni J, Zhong N, Wang M, Yan Y, Song D, Zhang Y, Zhang X, Ruian W, Cao S, Shao W (2024) Characterization and spatial analysis of coseismic landslides triggered by the Luding Ms 6.8 earthquake in the Xianshuihe fault zone, Southwest China. J Mount Sci 21(1):160–181. https://doi.org/10.1007/s11629-023-8291-3

Hao J, Ji C, Wang W, Yao Z (2013) Rupture history of the 2013 Mw 6.6 Lushan earthquake constrained with local strong motion and teleseismic body and surface waves. Geophys Res Lett 40(20):5371–5376. https://doi.org/10.1002/2013GL056876

Harp EL, Jibson RW, Schmitt RG (2016) Map of landslides triggered by the January 12, Haiti earthquake: U. S. Geological Survey Scientific Investigations Map. 3353, 15 p., 1 sheet, scale 1: 150 000. https://doi.org/10.3133/sim3353.

Hartmann J, Moosdorf N (2012) The new global lithological map database GLiM: a representation of rock properties at the Earth surface. Geochem Geophys Geosyst. https://doi.org/10.1029/2012GC004370

Havenith HB, Torgoev A, Braun A, Schlögel R, Micu M (2016) A new classification of earthquake-induced landslide event sizes based on seismotectonic, topographic, climatic and geologic factors. Geoenvir Disast 3:2–24. https://doi.org/10.1186/s40677-016-0041-1

Havenith H-B, Guerrier K, Schlögel R, Braun A, Ulysse S, Mreyen A-S, Victor K-H, Saint-Fleur N, Cauchi L, Boisson D, Prépetit C (2022) Earthquake-induced landslides in Haiti: analysis of seismotectonic and possible climatic influences. Nat Hazards Earth Syst Sci 22:3361–3384. https://doi.org/10.5194/nhess-22-3361-2022

He Q, Wang M, Liu K (2021) Rapidly assessing earthquake-induced landslide susceptibility on a global scale using random forest. Geomorphology 391:107889. https://doi.org/10.1016/j.geomorph.2021.107889

Houqun C, Shengxin W, Faning D (2016) Seismic safety of high arch dams. Pp 53–81. ISBN 978–0–12–803628–0, https://doi.org/10.1016/C2013-0-19380-4.

Hsieh S-Y, Lee C-T (2011) Empirical estimation of the Newmark displacement from the Arias intensity and critical acceleration. Eng Geol 122(1–2):34–42. https://doi.org/10.1016/j.enggeo.2010.12.006

Hsu TY, Pratomo A (2022) Early peak ground acceleration prediction for on-site earthquake early warning using LSTM neural network. Front Earth Sci 10:911947. https://doi.org/10.3389/feart.2022.911947

Huang B-S (2000) Two-dimensional reconstruction of the surface ground motions of an earthquake: the September 21, 1999, Chi-Chi, Taiwan Earthquake. Geophys Res Lett 27:3025. https://doi.org/10.1029/2000GL011481

Huang D, Wang G, Du C, Jin F, Feng K, Chen Z (2020) An integrated SEM-Newmark model for physics-based regional coseismic landslide assessment. Soil Dyn Earthq Eng 132:106066. https://doi.org/10.1016/j.soildyn.2020.106066

Huo J, Hu Y (1992) Study on attenuation laws of ground motion parameters. Earth. Eng. Vibration 12:1–11

Hussain S, Pan B, Afzal Z et al (2023) Landslide detection and inventory updating using the time-series InSAR approach along the Karakoram Highway. Northern Pakistan Sci Rep 13:7485. https://doi.org/10.1038/s41598-023-34030-0

Idriss IM (2008) An NGA empirical model for estimating the horizontal spectral values generated by shallow crustal earthquakes. Earthq Spectra 24:217–242. https://doi.org/10.1193/1.2924362

Ingles J, Darrozes J, Soula J-C (2006) Effects of the vertical component of ground shaking on earthquake-induced landslide displacements using generalized Newmark analysis. Eng Geol 86(2–3):134–147. https://doi.org/10.1016/j.enggeo.2006.02.018

Jang D, Ahn J-K, Kim T-W, Kwak DY (2023) Linearly combined ground motion model using quadratic programming for low- to mid-size seismicity region: South Korea. Front Earth Sci. https://doi.org/10.3389/feart.2022.1067802

Jibson RW (1993) Predicting earthquake-induced landslide displacements using Newmark's sliding block analysis. Transp Res Rec 1411:9–17

Jibson RW (2007) Regression models for estimating coseismic landslide displacement. Eng Geol 91(2/4):209–218. https://doi.org/10.1016/j.enggeo.2007.01.013

Jibson RW (2011) Methods for assessing the stability of slopes during earthquakes-a retrospective. Eng Geol 122:43–50. https://doi.org/10.1016/j.enggeo.2010.09.017

Jibson RW, Keefer DK (1993) Analysis of the seismic origin of landslides: examples from the New Madrid seismic zone. Geol Soc Am Bull 105(4):521–536

Jibson RW, Harp EL, Michael JA (2000) A method for producing digital probabilistic seismic landslide hazard maps. Eng Geology 58(3–4):271–289. https://doi.org/10.1016/s0013-7952(00)00039-9

Jibson RW, Harp EL, Schulz W, Keefer DK (2004) Landslides triggered by the 2002 M-7.9 Denali Fault, Alaska, earthquake and the inferred nature of the strong shaking. Earthq Spectra 20:669–691. https://doi.org/10.1193/1.1778173

Jibson RW, Harp EL, Schulz W, Keefer DK (2006) Large rock avalanches triggered by the M 7.9 Denali fault, Alaska, earthquake of 3 November 2002. Eng Geol 83(1):144–160

Jibson RW, Harp EL, Michael JA (1998) A method for producing digital probabilistic seismic landslide hazard maps: an example from the Los Angeles, California area. USGS Open-file report, pp 98–113. https://doi.org/10.1016/S0013-7952(00)00039-9.

Jin JL, Wang Y, Gao D, Yuan RM, Yang XY (2018) New evaluation models of Newmark displacement for Southwest China. Bull Seismol Soc Am 108(4):2221–2236. https://doi.org/10.1785/0120170349

Jin KP, Yao LK, Cheng QG et al (2019) Seismic landslides hazard zoning based on the modified Newmark model: a case study from the Lushan earthquake, China. Nat Hazards 99:493–509. https://doi.org/10.1007/s11069-019-03754-6

Jongmans D, Campillo M (1990) The Liège earthquake of November 8, 1983, Damage distribution and site effects. Earthq Spectra 6(4):713–737

Keefer DK (2002) Investigating landslides caused by earthquakes–a historical review. Surv Geophys 23:473–510. https://doi.org/10.1023/A:1021274710840

Kharismalatri HS, Ishikawa Y, Gomi T, Sidle RC, Shiraki K (2019) Evaluating factors for controlling sediment connectivity of landslide materials: a flume experiment. Water 11:17. https://doi.org/10.3390/w11010017

Khazai B, Sitar N (2004) Evaluation of factors controlling earthquake-induced landslides caused by Chi-Chi earthquake and comparison with the Northridge and Loma Prieta events. Eng Geol 71:1–2. https://doi.org/10.1016/S0013-7952(03)00127-3

Kocel E, Stewart RR, Mann P, Chang L (2016) Near-surface geophysical investigation of the 2010 Haiti earthquake epicentral area: Léogâne, Haiti. Interpretation 4(1):T49–T61. https://doi.org/10.1190/INT-2015-0038.1

Li WL, Huang RQ, Xu Q, Tang C (2013) Rapid susceptibility mapping of co-seismic landslides triggered by the 2013 Lushan Earthquake using the regression model developed for the 2008 Wenchuan Earthquake. J Mt Sci 10(5):699–715. https://doi.org/10.1007/s11629-013-2786-2

Li G, West AJ, Densmore AL, Hammond DE, Jin Z, Zhang F, Wang J, Hilton RG (2016) Connectivity of earthquake-triggered landslides with the fluvial network: implications for landslide sediment transport after the 2008 Wenchuan earthquake. J Geophys Res Earth Surf 121:703–724. https://doi.org/10.1002/2015JF003718

Li M, Wu P, Sexton DMH, Ma Z (2021a) Potential shifts in climate zones under a future global warming scenario using soil moisture classification. Clim Dyn 56:2071–2092. https://doi.org/10.1007/s00382-020-05576-w

Li Y, Cui P, Ye C, Junior JM, Zhang Z, Guo J, Li J (2021b) Accurate prediction of earthquake-induced landslides based on deep learning considering landslide source area. Remote Sens 13(17):3436. https://doi.org/10.3390/rs13173436

Li Y, Ming D, Zhang L, Niu Y, Chen Y (2024a) Seismic landslide susceptibility assessment using Newmark Displacement based on a dual-channel convolutional neural network. Remote Sens 16:566. https://doi.org/10.3390/rs16030566

Li Y, Wang G, Ding Y (2024b) Nonlinear seismic response analysis of slopes considering the coupled effect of slope geometry and soil stratigraphy. Geophys J Int 238(1):616–630. https://doi.org/10.1093/gji/ggae174

Liao HW, Lee CT (2000) Landslides triggered by the Chi-Chi earthquake. In: Proceedings of the 21st Asian Conference on Remote Sensing, Taipei. 1–2: 383–388.

Lin CW, Liu SH, Lee SY, Liu CC (2006) Impacts of the Chi-Chi earthquake on subsequent rainfall-induced landslides in central Taiwan. Eng Geol 86:87–101. https://doi.org/10.1016/j.enggeo.2006.02.010

Lin G-W, Chen H, Chen Y-H, Horng M-J (2008) Influence of typhoons and earthquakes on rainfall-induced landslides and suspended sediments discharge. Eng Geol 97:32–41. https://doi.org/10.1016/j.enggeo.2007.12.001

Lin C-W, Chen W-S. (2016). Geologic Map of Taiwan Geological Society of Taiwan.

Loche M, Scaringi G, Yunus AP et al (2022) Surface temperature controls the pattern of post-earthquake landslide activity. Sci Rep 12:988. https://doi.org/10.1038/s41598-022-04992-8

Luo Y, Zhao L, Zeng X, Gao Y (2015) Focal mechanisms of the Lushan earthquake sequence and spatial variation of the stress field. Sci China Earth Sci 58(7):1148–1158. https://doi.org/10.1007/s11430-014-5017-y

M.A. (1991). Global geomorphology: an introduction to the study of landforms. Pearson, Prentice Hall, England, 537 pp.

Ma S, Xu C (2019) Assessment of co-seismic landslide hazard using the Newmark model and statistical analyses: a case study of the 2013 Lushan, China, Mw6.6 earthquake. Nat Hazards 96:389–412. https://doi.org/10.1007/s11069-018-3548-9

Ma KF, Mori J, Lee SJ, Yu SB (2001) Spatial and temporal distribution of slip for the 1999 Chi-Chi, Taiwan, earthquake. Bull Seismol Soc Am 91(5):1069–1087

Marc O, Hovius N (2015) Amalgamation in landslide maps: effects and automatic detection. Nat Hazards Earth Syst Sci Discuss 15(15):723–733. https://doi.org/10.5194/nhess-15-723-2015

Merz HA, Cornell CA (1973) Seismic risk analysis based on a quadratic magnitude-frequency law. Bullet Seismol Soc Am 63(6–1):1999–2006. https://doi.org/10.1785/BSSA0636-11999

Meunier P, Hovius N, Haines JA (2008) Topographic site effects and the location of earthquake induced landslides. Earth Planet Sci Lett 275(3–4):221–232

Miles SB, Ho CL (1999) Rigorous landslide hazard zonation using Newmark's method and stochastic ground motion simulation. Soil Dyn Earthq Eng

Moore ID, Grayson RB, Ladson AR (1991) Digital terrain modelling: a review of hydrological, geomorphological, and biological applications. Hydrol Process 5(1):3–30

Newmark NM (1965) Effects of earthquakes on dams and embankments. Géotechnique 15:139–160. https://doi.org/10.1680/geot.1965.15.2.139

Notti D, Cignetti M, Godone D, Giordan D (2023) Predicting deep-seated landslide displacement on Taiwan's Lushan through the integration of convolutional neural networks. Nat Hazard 23(7):2625–2648. https://doi.org/10.5194/nhess-23-2625-2023

Oliveti I, Faenza L, Michelini A (2022) New reversible relationships between ground motion parameters and macroseismic intensity for Italy and their application in ShakeMap. Geophys J Int 231:1117–1137. https://doi.org/10.1093/gji/ggac245

Possee D, Keir D, Harmon N, Rychert C, Eakin C et al (2020) Spatial variations in crustal and mantle anisotropy across the north American-Caribbean Boundary on Haiti. J Geophys Res Solid Earth. https://doi.org/10.1029/2019JB018438

Power M, Chiou B, Abrahamson N, Bozorgnia Y, Shantz T, Roblee C (2012) An overview of the NGA Project. Earthq Spect 24:3–21

Prentice CS, Mann P, Crone AJ, Gold RD, Hudnut KW, Briggs RW, Koehler RD, Jean P (2010) Seismic hazard of the Enriquillo-Plantain Garden fault in Haiti inferred from palaeoseismology. Nat Geosci 3:789–793. https://doi.org/10.1038/ngeo991

Pudasaini SP, Krautblatter M (2021) The mechanics of landslide mobility with erosion. Nat Commun 12:6793. https://doi.org/10.1038/s41467-021-26959-5

Pyakurel A, Diwakar KC, Dahal BK (2024) Enhancing co-seismic landslide susceptibility, building exposure, and risk analysis through machine learning. Sci Rep. https://doi.org/10.1038/s41598-024-54898-w

Qi S, Qiang X, Lan H, Zhang B, Liu J (2010) Spatial distribution analysis of landslides triggered by 2008.5.12 Wenchuan Earthquake, China. Eng Geol 116(1–2):95–108. https://doi.org/10.1016/j.enggeo.2010.07.011

Rathje EM, Saygili G (2009) Probabilistic assessment of earthquake-induced sliding displacements of natural slopes. Bull NZ Soc Earthq Eng 42:18–27. https://doi.org/10.5459/bnzsee.42.1.18-27

Richardson E, Marone C (2008) What triggers tremor? Science 319(5860):166–167. https://doi.org/10.1126/science.1152877

Robinson TR, Rosser NJ, Densmore AL (2017) Rapid post-earthquake modelling of coseismic landslide intensity and distribution for emergency response decision support. Nat Hazards Earth Syst Sci 17:1521–1540. https://doi.org/10.5194/nhess-17-1521-2017

Rodríguez-Peces MJ, García-Mayordomo J, Azañón JM et al (2014) GIS application for regional assessment of seismically induced slope failures in the Sierra Nevada Range, South Spain, along the Padul Fault. Environ Earth Sci 72:2423–2435. https://doi.org/10.1007/s12665-014-3151-7

Shao X, Xu C, Ma S (2022a) Preliminary analysis of coseismic landslides induced by the 1 June 2022 Ms 6.1 Lushan earthquake, China. Sustainability 14:16554. https://doi.org/10.3390/su14241655

Shao X, Xu C, Wang P, Li L, He X, Chen Z, Huang Y, Xu X (2022b) Two public inventories of landslides induced by the 10 June 2022 Maerkang Earthquake swarm, China and ancient landslides in the affected area. Nat Hazards Res. https://doi.org/10.1016/j.nhres.2022.09.001

Tang D, Ge W, Cao X (2023) Stress triggering of the 2022 Lushan-Maerkang earthquake sequence by historical events and its implication for fault stress evolution in eastern Tibet. Front Earth Sci 11:1105394. https://doi.org/10.3389/feart.2023.1105394

Tseng C-M, Chen Y-R, Chang C-M, Yang Y-L, Chen Y-R, Hsieh S-C (2022) Statistical analysis of the potential of landslides induced by combination between rainfall and earthquakes. Water 14(22):3691. https://doi.org/10.3390/w14223691

Tsinidis G, Di Sarno L, Sextos A, Furtner P (2019) A critical review on the vulnerability assessment of natural gas pipelines subjected to seismic wave propagation. Part 1: fragility relations and implemented seismic intensity measures. Tunn Undergr Space Technol 86:279–296. https://doi.org/10.1016/j.tust.2019.01.025

Valagussa A, Marc O, Frattini P, Crosta GB (2019) Seismic and geological controls on earthquake-induced landslide size. Earth Planet Sci Lett 506:268–281. https://doi.org/10.1016/j.epsl.2018.11.005

Wan W, Bo J, Qi W, Peng D, Li Q, Duan Y (2022) Analysis of peak ground acceleration attenuation characteristics in the Pazarcik earthquake, Türkiye. Appl Sci 13(20):11436. https://doi.org/10.3390/app132011436

Wang K-L, Lin M-L (2010) Development of shallow seismic landslide potential map based on Newmark's displacement: the case study of Chi-Chi earthquake. Taiwan Environ Earth Sci 60(4):775–785. https://doi.org/10.1007/s12665-009-0215-1

Wang M, Liu M, Yang S, Shi P (2014) Incorporating triggering and environmental factors in the analysis of earthquake-induced landslide hazards. Int J Disaster Risk Sci 5(2):125–135. https://doi.org/10.1007/s13753-014-0020-7

Wang G, Du C, Huang D, Jin F, Koo RCH, Kwan Julian SH (2018) Parametric models for 3D topographic amplification of ground motions considering subsurface soils. Soil Dyn Earthq Eng 115:41–54
Ward TJ, Li R-M, Simons DB (1982) Mapping landslide hazards in forest watersheds. J Geotech Eng Div 108(2):319–324. https://doi.org/10.1061/AJGEB6.0001250
Wen BP, Wang SJ, Wang EZ et al (2004) Characteristics of rapid giant landslides in China. Landslides 1:247–261. https://doi.org/10.1007/s10346-004-0022-4
White AF, Brantley SL (2003) The effect of time on the weathering of silicate minerals: why do weathering rates differ in the laboratory and field? Chem Geol 202(3–4):479–506. https://doi.org/10.1016/j.chemgeo.2003.03.001
Wilson RC, Keefer DK (1983) Dynamic analysis of a slope failure from the 6 August 1979 Coyote Lake, California, earthquake. Bull Seismol Soc Am 73(3):863–877. https://doi.org/10.1785/BSSA0730030863
Wu C-H, Kuo Y-H (1999) Rainfall simulation associated with typhoon herb (1996) near Central Taiwan. Weather Forecast 17(5):1001–1017
Wu X, Xu X, Yu G, Ren J, Yang X, Chen G, Xu C, Du K, Huang X, Yang H, Li K, Hao H (2023) China active faults database and its web system. Earth Syst Sci Data. https://doi.org/10.5194/essd-2023-119
XiWei X, Wen X, Han ZJ, Chen GH, Li CY, Zheng WJ, Zhnag SM, Ren ZQ, Chong X, Tan XB, Wei ZY, Wang MM, Ren JJ, He ZT, Liang MJ (2013) Lushan M S7.0 earthquake: a blind reserve-fault event. Chin Sci Bullet 58(28–29):3437–3443. https://doi.org/10.1007/s11434-013-5999-4
Xu Z, Ji S, Li H, Hou L, Fu X, Cai Z (2008) Uplift of the Longmen Shan range and the Wenchuan earthquake. Episodes 31(3):291–301
Xu C, Shyu JBH, Xu X (2014) Landslides triggered by the 12 January 2010 Port-au-Prince, Haiti, MwD7:0 earthquake: visual interpretation, inventory compiling, and spatial distribution statistical analysis. Nat Hazards Earth Syst Sci 14:1789–1818. https://doi.org/10.5194/nhess-14-1789-2014
Yang C-M, Dong J-J, Lee C-T et al (2024) Revisit the classical Newmark displacement analysis for earthquake-induced wedge sliding of a rock slope. Engi Geol 328(2024):107374. https://doi.org/10.1016/j.enggeo.2023.107374
Yao X, Qi S, Liu C, Guo S, Huang X, Xu C et al (2020) An empirical attenuation model of the peak ground acceleration (PGA) in the near field of a strong earthquake. Nat Hazards. https://doi.org/10.1007/s11069-020-04332-x
Yiğit A (2020) Prediction of amount of earthquake-induced slope displacement by using Newmark method. Eng Geol 264:105385. https://doi.org/10.1016/j.enggeo.2019.105385
Yuan RM, Deng QH, Cunningham D, Xu C, Xu XW, Chang CP (2013) Density distribution of landslides triggered by the 2008 Wenchuan earthquake and their relationships to peak ground acceleration. Bull Seismol Soc Am 103:2344–2355
Yuan R, Deng Q, Cunningham D, Han Z, Zhang D, Zhang B (2016) Newmark displacement model for landslides induced by the 2013 Ms 7.0 Lushan earthquake, China. Front Earth Sci 10(4):740–750. https://doi.org/10.1007/s11707-015-0547-y
Zevenbergen LW, Thorne CR (1987) Quantitative analysis of land surface topography. Earth Surf Proc Land 12(1):47–56
Zhang P-Z (2013) A review on active tectonics and deep crustal processes of the Western Sichuan region, eastern margin of the Tibetan Plateau. Tectonophysics 584:7–22. https://doi.org/10.1016/j.tecto.2012.02.021
Zhang Y, Jin Z, Liang D (2023) Fuzzy logic regional landslide susceptibility multi-field information map representation analysis method constrained by spatial characteristics of mining factors in mining areas. Processes 11(4):985
Zhao B, Li W, Su L, Wang Y, Wu H (2022) Insights into the landslides triggered by the 2022 Lushan Ms 6.1 earthquake: spatial distribution and controls. Remote Sens 14:4365. https://doi.org/10.3390/rs14174365
Zhao B, Su L, Xu Q, Li W, Xu C, Wang Y (2023) A review of recent earthquake-induced landslides on the Tibetan Plateau. Earth Sci Rev 244:104534. https://doi.org/10.1016/j.earscirev.2023.104534